

Kaon production and propagation at intermediate relativistic energies*

A.B. Larionov^{1,2} and U. Mosel¹

¹*Institut für Theoretische Physik, Universität Giessen, D-35392 Giessen, Germany*

²*RRC "I.V. Kurchatov Institute", 123182 Moscow, Russia*

(Dated: July 23, 2018)

Abstract

We systematically study K^+ observables in nucleus-nucleus collisions at 1-2 A GeV within the Boltzmann-Uehling-Uhlenbeck (BUU) transport model. We compare our calculations with the KaoS data on the kaon multiplicities and spectra. In addition, the kaon collective flow is computed and compared with the FOPI and KaoS data. We show, that the elliptic kaon flow measured recently by the KaoS Collaboration is best described by using the Brown-Rho parametrization of the kaon potential ($U_K(\rho_0) \simeq 30$ MeV).

PACS numbers: 24.10.Jv; 24.10.Lx; 25.75.Dw; 25.75.Ld

* Work supported by GSI Darmstadt

I. INTRODUCTION

Since about 20 years strangeness production in heavy-ion collisions is a hot topic of theoretical and experimental studies. Due to rather high energy thresholds in NN collisions ($E_{beam} = 1.58$ GeV for $NN \rightarrow K\Lambda N$ and $E_{beam} = 2.5$ GeV for $NN \rightarrow NNK\bar{K}$) the secondary processes $\Delta N \rightarrow KYN$, $\pi N \rightarrow KY$ and $\pi Y \rightarrow \bar{K}N$ – which require high baryon density – are important in the case of nucleus-nucleus collisions at 1-2 A GeV. Moreover, due to the relatively low (~ 10 mb) KN scattering cross section and the absence of the absorption channel of a kaon on a nucleon in strong interactions, nuclear matter is practically transparent for kaons [1]. Thus, the kaon yield is a good probe for the nuclear equation-of-state (EOS). This idea has originally been proposed and tested in BUU calculations by Aichelin and Ko in Ref. [2]. Recently it has been shown by Fuchs et al. [3] within the Tübingen QMD model, that the ratio of the kaon yields in Au+Au and C+C collisions plotted vs the beam energy favours a soft EOS ($K=200$ MeV) when comparing with the KaoS data [4]. This ratio seems to be weakly sensitive to the experimentally not measurable $\Delta N \rightarrow KYN$ cross section and to the choice of the kaon potential and serves as a good probe for the nuclear EOS.

Another direction of studies is related to the kaon and antikaon propagation in the nuclear medium [5, 6, 7, 8, 9, 10, 11, 12]. For these studies the K and \bar{K} mean field potentials play a crucial role. In the lowest order approximation to the chiral Lagrangian the kaon (antikaon) potential has an attractive scalar and a repulsive (attractive) vector part [6, 13, 14]. This leads to a weakly repulsive potential ($U_K(\rho_0) \simeq 7$ MeV, where $\rho_0 = 0.17 \text{ fm}^{-3}$) for kaons and a strongly attractive potential ($U_{\bar{K}}(\rho_0) \simeq -100$ MeV) for antikaons. The kaon [5, 6] and the antikaon [8] in-plane flows and the kaon azimuthal distributions [7] are strongly influenced by the K and \bar{K} potentials. The authors of Ref. [9] have shown within the HSD model, that a repulsive potential ($U_K(\rho_0) \simeq 30$ MeV) seems to be needed for description of the first FOPI data [15] on the K^+ in-plane flow. In the most recent HSD analysis of Ref. [12], where different kaon potentials were tested, the one given by the chiral perturbation theory in the relativistic Hartree approximation ($U_K(\rho_0) \simeq 20$ MeV) was found to give the best agreement with the kaon flow data. The same value of the kaon potential at normal nuclear matter density ($U_K(\rho_0) = 20 \pm 5$ MeV) was reported in a recent CBUU analysis of the K^+ production in proton-nucleus reactions by Rudy et al. [16].

In the approaches of Refs. [5, 6, 7, 9, 12, 16] the spatial components of the vector field in the kaon potential were neglected which should be approximately valid in a central zone of a symmetric colliding system where the baryon current disappears. The spatial components were taken into account by Fuchs et al. [17] within the Tübingen QMD model and led to a much smaller negative flow of K^+ 's. This is a consequence of the cancellation effect of the repulsive time component of the kaon vector field by the Lorentz force generated by the space components of the kaon vector field [17]. However, the calculations of Ref. [10], where the spatial components have also been taken into account, have produced a larger negative kaon flow, which disagrees with Ref. [17]. The latest calculations by the Tübingen QMD group [11] have corroborated their earlier analysis [17] and demonstrated that the new FOPI data on the kaon in-plane flow [18] are best described by using the kaon potential given by the Brown-Rho (BR) parametrization [19] ($U_K(\rho_0) \simeq 30$ MeV). At $\rho \leq \rho_0$ the kaon potential in the BR parametrization is close to the one in the impulse approximation (c.f. Refs. [6, 20]). Recent self-consistent calculations of Refs. [21, 22] show even stronger repulsion for kaons ($U_K(\rho_0) = 36$ MeV in Ref. [21] and $U_K(\rho_0) = 39$ MeV in Ref. [22]).

The K^\pm azimuthal distributions at midrapidity (squeeze-out) have also been studied within an earlier version of the Tübingen QMD model in Ref. [23]. It has been concluded in [23], that the K^+ squeeze-out is caused mainly by the repulsive K^+ potential. However, the quantitative agreement with experimental data for Au+Au at 1 A GeV [24] was achieved only with the static kaon potential in [23]. The Lorentz force, as has been concluded in [23], destroys the agreement with the data by reducing the K^+ squeeze-out signal strongly (we will come back to this point later on).

The present work is an attempt to describe the K^+ data on multiplicities and phase space distributions at the beam energies of 1-2 A GeV [4, 18, 24, 25, 26, 27, 28, 29] on the basis of a BUU model [30, 31, 32]. The BUU model [30, 31, 32] includes a large set of the baryonic resonances (see the next Section). Due to the channels $NR \rightarrow KYN$ and $NR \rightarrow K\bar{K}NN$, where R stands for a nonstrange baryon resonance, the resonances enhance strangeness production. Thus, despite of many previous transport theoretical studies on the strangeness production at SIS energies (c.f. Refs. [2, 3, 5, 6, 7, 8, 9, 10, 11, 12, 33, 34]) it would be interesting to confront also our calculations with experimental data, since, e.g., the QMD models [3, 10, 11, 33, 34, 35, 36] propagate only $\Delta(1232)$ and $N^*(1440)$ resonances and the HSD model [9, 12, 37] propagates only $\Delta(1232)$, $N^*(1440)$ and $N^*(1535)$ resonances

(see also Ref. [38] for the comparison of the different transport calculations).

The main purpose of our study is to clarify whether a kaon potential is actually needed to describe the data and, if so, how strong it must be. In particular, we will analyse the recent KaoS data [29] on the kaon azimuthal distributions.

In Sect. II a brief description of the BUU model is given. Sect. III contains the results of numerical calculations. In Sect. IV we summarize our results and draw some conclusions.

II. THE BUU MODEL

Our calculations are based on the BUU model in the version described in Refs. [30, 31, 32]. The model explicitly propagates all N^* and Δ resonances that are rated with at least 2 stars in the analysis of Ref. [39], which includes the N^* states $P_{11}(1440)$, $D_{13}(1520)$, $S_{11}(1535)$, $S_{11}(1650)$, $D_{15}(1675)$, $F_{15}(1680)$, $P_{13}(1879)$, $F_{17}(1990)$, $G_{17}(2190)$ and the Δ states $P_{33}(1232)$, $P_{33}(1600)$, $S_{31}(1620)$, $S_{31}(1900)$, $F_{35}(1905)$, $P_{31}(1910)$, $D_{35}(1930)$, $F_{37}(1950)$, $D_{35}(2350)$. Also the $S = -1$ baryons $Y = \Lambda(1116)$, $\Sigma(1189)$ and $Y^* = S_{01}(1405)$, $D_{03}(1520)$, $P_{01}(1600)$, $S_{01}(1670)$, $D_{03}(1690)$, $S_{01}(1800)$, $P_{01}(1810)$, $F_{05}(1820)$, $D_{05}(1830)$, $P_{03}(1890)$, $G_{07}(2100)$, $F_{05}(2110)$, $P_{13}(1385)$, $P_{11}(1660)$, $D_{13}(1670)$, $S_{11}(1750)$, $D_{15}(1775)$, $F_{15}(1915)$, $F_{17}(2030)$ are propagated explicitly in the model. The Y^* -resonances are the intermediate states of the strangeness exchange reactions $\pi Y \leftrightarrow Y^* \leftrightarrow \bar{K} N$.

In the meson sector, the following particles are propagated: π , η , ρ , σ , ω , η' , ϕ , η_c , J/ψ , K , \bar{K} , K^* , \bar{K}^* . Also the cascades, charmed baryons and mesons are propagated, which are, however, irrelevant degrees of freedom at SIS energies.

The model has been successfully applied to γ and e^- induced reactions on nuclei [30, 40] and to the description of the collective nucleon flows in heavy-ion collisions at 0.1-2 A GeV [41]. The reproduction of the pion abundancies in heavy-ion collisions at SIS energies requires, however, to apply the in-medium reduced resonance production/absorption cross sections $NN \leftrightarrow NR$ [32, 42]. We will drop the detailed description of the model which can be found in Refs. [30, 31, 32] concentrating here only on some novel features related to strangeness production.

For kaon production in baryon-baryon collisions we include the following channels: $NN \rightarrow NYK$, $NN \rightarrow \Delta YK$, $\Delta N \rightarrow NYK$, $\Delta N \rightarrow \Delta YK$ and $\Delta\Delta \rightarrow \Delta YK$, where $\Delta \equiv P_{33}(1232)$ and $Y = \Lambda(1115)$ or $\Sigma(1189)$, with all possible isospin combinations of the incoming and

the outgoing particles. The channel $\Delta\Delta \rightarrow NYK$ is not included, since it is possible only through an exchange by an on-shell pion [43], which is already included in BUU via the consecutive $\Delta \leftrightarrow N\pi$ and $\pi B \rightarrow KY$ processes, where $B \equiv N$ or R . The isospin-dependent parametrizations for the cross sections of kaon production in the NN , $N\Delta$ and $\Delta\Delta$ collisions are taken from Ref. [43]. In addition, we allow to produce a kaon-hyperon pair in a collision between any two nonstrange baryons: cross sections of these processes are obtained from the cross sections of Ref. [43] by replacing an incoming N^* resonance by the nucleon and an incoming higher Δ resonance by the $\Delta(1232)$ for the same \sqrt{s} . The $K\bar{K}$ pair production in a baryon-baryon collision $BB \rightarrow N NK\bar{K}$ is also included via cross sections parametrized in Ref. [44].

The pion-baryon collisions $\pi B \rightarrow YK$ also contribute quite significantly to the strangeness production in heavy-ion collisions. If the incoming baryon B is a nucleon or a $\Delta(1232)$ -resonance, the cross sections from Ref. [45] are applied. If $B = N^*$ or higher Δ , it is substituted by the nucleon or $\Delta(1232)$ -resonance, depending on the isospin, and then the corresponding cross sections from Ref. [45] are used. The $\pi B \rightarrow NK\bar{K}$ process is taken into account with a cross section parametrized in Ref. [46]. The kaon elastic, including charge exchange, and inelastic scattering processes $KN \rightarrow KN$ and $KN \rightarrow KN\pi$ are also taken into account: their cross sections are fitted to the data [47] (see Ref. [31]).

Since in the present work we concentrate on the kaon production at energies below 2 A GeV, the kaon production channels $BB \rightarrow NYK$ and $\pi B \rightarrow YK$ are those relevant for our study. The reactions including antikaons play, practically, no role for kaon production (see Table I below). The kaon production is treated perturbatively and the FRITIOF mechanism is switched off in this work, since the kaon multiplicity per nucleus-nucleus collision is still quite small at the considered beam energies (see Fig. 2 below).

In our calculations the nucleons are propagated in a Skyrme-like mean field including the momentum-dependent part (c.f. Ref. [41]). Most of the calculations are done with a soft momentum-dependent mean field (SM, $K = 220$ MeV). When, for comparison, also a hard momentum-dependent mean field (HM, $K = 380$ MeV) is used, this will be mentioned in the text below. It is assumed that all the nonstrange baryonic resonances experience the same mean field as nucleons. For the hyperons, according to the fraction of the nonstrange quarks, we apply the nucleon mean field multiplied by 2/3 [3, 37, 48].

The K^\pm single-particle energies are expressed as

$$\omega_K^\pm(\mathbf{k}) = \pm V^0 + \sqrt{\mathbf{k}^{*2} + m_K^{*2}} , \quad (1)$$

$\mathbf{k}^* = \mathbf{k} \mp \mathbf{V}$ is the kaon kinetic momentum, $V^\mu = (V^0, \mathbf{V})$ is the kaon vector field and m_K^* is the kaon effective (Dirac) mass. According to Refs. [11, 19], the kaon effective mass and the kaon vector field are given by the following expressions :

$$m_K^* = \sqrt{m_K^2 - \frac{\Sigma_{KN}}{f_\pi^2} \rho_s + V^2} , \quad (2)$$

$$V^\mu = \frac{3}{8f_\pi^{*2}} j^\mu , \quad (3)$$

where $m_K = 0.496$ GeV is the bare kaon mass, ρ_s and j^μ are the baryon scalar density and the four-current, respectively. The parameters which appear in Eqs. (2),(3) are $\Sigma_{KN} = 0.450$ GeV — the kaon-nucleon sigma term, $f_\pi = 0.093$ GeV — the vacuum pion decay constant and $f_\pi^* = \sqrt{0.6} f_\pi$ — the in-medium pion decay constant at normal nuclear matter density ρ_0 [19].

Using the in-medium pion decay constant rather than the vacuum one in Eq. (3) leads to the desirable consequence [19], that the resulting kaon vector potential (3) is just 1/3 of the nucleon vector potential given by the relativistic mean field model. In the scalar term $\propto \rho_s$ (Eq. (2)) the vacuum pion decay constant is used, since for kaons the higher order (range) term in the chiral expansion cancels an effect of the in-medium pion decay constant in this case [19]. The cancellation, however, does not take place for the antikaons [19]. Thus, Eq.(2) can be considered for the antikaons as a phenomenological parametrization, which, nevertheless, leads to reasonable values of the \bar{K} potential (see below).

The kaon (antikaon) potential $U_{K(\bar{K})}$ is defined as

$$U_{K(\bar{K})}(\mathbf{k}) = \omega_K^\pm(\mathbf{k}) - \sqrt{\mathbf{k}^2 + m_K^2} . \quad (4)$$

Following Ref. [11], we will denote the kaon (antikaon) potential with parameters determined above as the BR potential which will be used as the default potential in our calculations. However, as in [11], we will perform for a comparison also some calculations applying the kaon (antikaon) potential with $\Sigma_{KN} = 0.350$ GeV and with the free pion decay constant f_π instead of f_π^* in the vector potential (3) which we call a Ko-Li (KL) potential [6].

Both choices of the kaon potential, BR and KL, are shown for the static case ($\mathbf{k} = 0$) in the upper panel of Fig. 1 as functions of the baryon density. The BR potential is strongly

repulsive ($U_K(\rho_0) = 32$ MeV), while the KL potential is much weaker ($U_K(\rho_0) = 6$ MeV). We have to point out here, that our potentials are slightly more repulsive at higher density than the corresponding potentials from Ref. [11] due to different versions of the relativistic mean field model used to evaluate the scalar density. For an orientation, we show in the lower panel of Fig. 1 the scalar density as a function of the baryon density which is given by the NL2 model [49] applied in our calculations. In the case of antikaons, the BR (KL) parametrization produces $U_{\bar{K}}(\rho_0) = -144$ MeV (-100 MeV).

In the BUU implementation we solve the Hamiltonian equations of motion for the kaon (antikaon) test particles, where the Hamilton function is the single-particle energy (1) which now implicitly depends also on space and time via the vector field $V^\mu(\mathbf{r}, t)$ and the effective mass $m_K^*(\mathbf{r}, t)$:

$$\dot{\mathbf{r}} = \frac{\partial \omega_K^\pm(\mathbf{k}, \mathbf{r}, t)}{\partial \mathbf{k}} = \frac{\mathbf{k}^*}{E^*}, \quad (5)$$

$$\dot{\mathbf{k}} = -\frac{\partial \omega_K^\pm(\mathbf{k}, \mathbf{r}, t)}{\partial \mathbf{r}} = -\frac{m_K^*}{E^*} \frac{\partial m_K^*}{\partial \mathbf{r}} \mp \frac{\partial V_0}{\partial \mathbf{r}} \pm \frac{k_\alpha^*}{E^*} \frac{\partial V_\alpha}{\partial \mathbf{r}}, \quad (6)$$

where $E^* = \sqrt{\mathbf{k}^{*2} + m_K^{*2}}$. These equations of motions are completely equivalent to those in the covariant form derived in Refs. [11, 17]. The last term in the r.h.s. of Eq.(6) is a velocity-dependent (Lorentz-like) force caused by the spatial components \mathbf{V} of the kaon vector field.

Potentials shift the particle production thresholds in nuclear medium. We take this effect into account, following Ref. [3], by replacing the bare center-of-mass (c.m.) energy $\sqrt{s_{free}}$ in the argument of the cross sections $\sigma_{BB \rightarrow \text{strangeness}}(\sqrt{s_{free}})$ and $\sigma_{\pi B \rightarrow \text{strangeness}}(\sqrt{s_{free}})$ by a corrected quantity. E.g., for the process $NN \rightarrow NYK$ we replace $\sqrt{s_{free}}$ by $\sqrt{s} - \tilde{m}_N - \tilde{m}_Y - \tilde{m}_K + m_N + m_Y + m_K$, where \sqrt{s} is the total in-medium c.m. energy of colliding particles including their mean field potentials, $\tilde{m}_X \equiv \varepsilon_X(\mathbf{p}_X^{c.m.} = 0)$ ($X = N, Y, K$) are the in-medium masses of the particles defined as their energies at rest in the c.m. frame of colliding particles [50].

In the simulation of a three-body phase space for the outgoing particles BYK ($B = N$ or $\Delta(1232)$ here) we use the kaon momentum distribution in the BYK c.m. frame proposed in Refs. [11, 51] :

$$dW_K \simeq \left(\frac{p}{p_{\max}} \right)^3 \left(1 - \frac{p}{p_{\max}} \right)^2, \quad (7)$$

where $p_{\max} = [(s - (\tilde{m}_B + \tilde{m}_Y)^2 + \tilde{m}_K^2)/4s - \tilde{m}_K^2]^{1/2}$ is the maximal kaon momentum in the

BYK c.m. frame. The angular distribution of the produced kaon is chosen in the empirical form [11, 52] : $d\sigma/d\cos\Theta_{c.m.} \propto (1 + a\cos^2\Theta_{c.m.})$ with $a = 1.2$ [52]. These two modifications lead to a softer kaon p_{lab} spectrum with respect to the simulation using an ideal Dalitz 3-body decay [11].

As it was demonstrated in Ref. [32], taking into account the Dirac masses of the baryons reduces the cross sections $NN \leftrightarrow NR$ in nuclear matter strongly, which brings our BUU calculations in a better agreement with the experimental data on pion multiplicities. In the calculations of the present work, if opposite is not stated explicitly, we use the in-medium cross sections $NN \leftrightarrow NR$ and $NN \leftrightarrow NN\pi$ [32] computed with the Dirac masses from the NL2 model [49]. The exchange pion collectivity effect and vertex corrections in the $NN \leftrightarrow N\Delta(1232)$ cross sections included in the calculations of Ref. [32] are neglected in the present work for simplicity. For brevity, we will call below a calculation employing the SM nucleon mean field, the BR kaon potential and the in-medium $NN \leftrightarrow NR$ cross sections the standard one.

III. NUMERICAL RESULTS

A. Kaon production channels

Before starting the comparison with experimental data, we have looked at the time evolution of the kaon number produced by the different channels, which is displayed in Fig. 2a,b,c for the central collisions Au+Au at 0.96 A GeV, Au+Au at 1.48 A GeV and Ni+Ni at 1.93 A GeV, respectively. Contributions of the channels to the total kaon number are summarized in Table I. In Fig. 2 and in Table I “ B ” in the initial state denotes N or R , while “ B ” in the final state denotes N or $\Delta(1232)$. The main kaon production channels are $RN \rightarrow BYK$, $NN \rightarrow BYK$ and $\pi B \rightarrow KY$. Other channels contribute all together on the level of $\sim 10\%$.

At the lowest energy of 0.96 A GeV the direct channel $NN \rightarrow NYK$ is deeply subthreshold and, thus, its contribution to the total kaon number is small. With increasing beam energy the contribution of the $NN \rightarrow NYK$ channel grows quickly, so that at 1.93 A GeV this channel becomes already the main one. The $RN \rightarrow BYK$ channel dominates at 0.96 and 1.48 A GeV. It is also the second important at 1.93 A GeV.

The $\pi B \rightarrow KY$ channel is the second important at 0.96 A GeV, but its contribution

decreases with increasing energy. This is quite natural, since a channel caused by secondary particles is energetically favourable at subthreshold energies. Another reason is that the pions are produced mainly in resonance decays $R \rightarrow N\pi$. The time scale of a nucleus-nucleus collision gets shorter with increasing beam energy. Therefore, more and more resonances will decay at the final low baryon density stage, when the probability of the pion-baryon collisions is small.

By comparing the time evolution of the kaon production (Fig. 2a,b,c) and of the central baryon density (Fig. 2d) we see that the largest rate of the kaon production takes place at about the time of the maximum compression. Thus, the kaon production delivers a signal from the highest compression stage of a heavy-ion collision without much distortion from the later stage, since kaons are not absorbed in the nuclear medium. This important kaon property has given, in particular, an opportunity to determine the nuclear EOS from the kaon yields [2, 3].

B. Kaon multiplicities and spectra

First, we check whether our model is able to reproduce the pion and kaon total multiplicities. Fig. 3 shows the inclusive multiplicities of π 's ($\pi = \pi^- + \pi^0 + \pi^+$) and K^+ 's per projectile nucleon for the systems Au+Au and C+C as functions of the beam energy in comparison to the data from Ref. [4]. In the calculations the particle multiplicities were impact parameter weighted in the region $b < 14$ fm for the Au+Au collisions and in the region $b < 5$ fm for the C+C collisions which corresponds to the geometrical cross sections. The pion multiplicity for the C+C system is well reproduced, except for the points at 1.8 and 2.0 A GeV, where we underpredict the data due to neglecting the string (FRITIOF) mechanism of particle production. In the case of Au+Au collisions our calculation produces too many pions at lower beam energies in spite of using the in-medium reduced $NN \leftrightarrow NR$ cross sections. Applying faster dropping Dirac masses of the baryons with nuclear density, e.g. given by the NL1 model [49], as well as taking into account the pion collectivity and vertex corrections in the $NN \leftrightarrow N\Delta(1232)$ cross sections [32] would lead to a better description of the pion multiplicity in the Au+Au case, however, at the cost of too low pion multiplicity for C+C collisions. The K^+ multiplicities are rather well reproduced for both systems Au+Au and C+C in the full SIS energy range.

Fig. 4 shows the laboratory momentum kaon spectra for the Au+Au collisions at 0.96 A GeV in comparison to the data [4]. The calculation without kaon potential (Fig. 4a, dashed lines with open up triangles) overestimates the kaon production strongly. The calculations, which include the kaon potential (Fig. 4a, BR — solid lines with open circles, KL — dotted lines with open squares) lead to a reduced lower momentum part of the spectra in better agreement with the data. The high momentum tail of the K^+ spectrum still remains too high in the calculations with the kaon potential.

In Fig. 4b we compare our standard calculation with the calculation employing the vacuum $NN \leftrightarrow NR$ cross sections. We see that dropping the in-medium corrections to the $NN \leftrightarrow NR$ cross sections results in about 50% larger kaon production cross section.

In order to see the origin of the produced kaons, we performed in Fig. 4c a channel decomposition of the laboratory momentum spectrum [53]. The largest contribution is provided by the pion-baryon collisions (πB). The nucleon- $\Delta(1232)$ and nucleon-higher resonance channels have also big contributions, comparable to the πB channel. This explains also a sensitivity of the kaon production cross section to the choice of the $NN \leftrightarrow NR$ cross sections (see Fig. 4b). The nucleon-nucleon collisions contribute only about 10% to the total kaon production cross section, since, at $E_{lab} = 0.96$ A GeV, they are mostly below the kaon production threshold.

In Fig. 4d we present a calculation with the HM nucleon mean field, which produces less K^+ 's (dashed line with open diamonds) than the standard calculation employing the SM mean field (solid line with open circles). The pion off-shellness effect [54] (dotted line with open squares) does not increase the K^+ multiplicity strong enough to bring the calculation with the HM mean field to agreement with the data.

Fig. 5 shows the laboratory momentum kaon spectra for the system C+C at 2 A GeV in comparison with the data from Ref. [52]. It is interesting that for this light system we reproduce rather well the slopes of the experimental spectra. A similar result was obtained earlier in Ref. [11] in a calculation with an anisotropic angular distribution of the produced kaon in a NN collision.

Fig. 6 shows the c.m. kinetic energy spectra of K^+ 's from Au+Au collisions at 1.5 A GeV for various event centrality classes. For the most central collisions, the calculation without potential (upper dashed line with open triangles) clearly overestimates kaon yield and also has a too steep slope. Including kaon potentials (BR — solid lines with open circles, KL —

dotted lines with open squares) reduces the kaon yield and reduces the steepness of the slope improving, thus, an agreement with the data for central events. With decreasing centrality the slopes of the spectra calculated with and without potentials get similar. This is expected since in peripheral events the compression is less and, therefore, any influence of the kaon potential is reduced. For the most central events we observe that the calculation employing the BR potential describes the data best, while for the peripheral events the calculation without potential is in best agreement with the data.

The qualitative trends presented in Fig. 6 can be better visible if one fits the spectra as follows [28]: $Ed^3\sigma/dp^3 = C \cdot E \cdot \exp(-E/T)$, where $E = E_{kin}^{cm} + m_K$ is the total energy of a kaon in the c.m. system. In the upper panel of Fig. 7 we show the inverse slope parameter T of the K^+ c.m. kinetic energy spectra as a function of a participant number A_{part} for the Au+Au system at 1.5 A GeV. The participant number was determined for each impact parameter from the geometrical overlap of colliding nuclei assuming sharp nuclear surfaces. As we already saw in Fig. 6, the difference between the inverse slope parameters from the calculations with and without kaon potentials is small at the peripheral collisions and increases with the collision centrality. The calculation with the KL potential provides the best description of the inverse slope parameter for all A_{part} .

The lower panel of Fig. 7 shows the K^+ multiplicity per participating nucleon as a function of A_{part} . The calculation without potential is above the data by a factor of two. The KL potential is not strong enough to get the correct multiplicities [55]. Only using the BR potential reduces the kaon multiplicity to a good agreement with the data.

Figs. 8 and 9 show, respectively, the K^+ transverse mass ($m_T \equiv \sqrt{p_T^2 + m^2}$) and c.m. rapidity spectra for Ni+Ni collisions at 1.93 A GeV in comparison to the data [26]. As in the case of Au+Au collisions at 1.5 A GeV we observe that the calculation without kaon potential overpredicts the kaon yields and produces too steep slopes at low m_T 's for the central collisions (left panels of Figs. 8 and 9). The BR potential provides the most reasonable description of the data for the central collisions. However, the steepness of the slopes is somewhat underestimated by the calculation with the BR potential. The slopes are, again, best described by the calculation with the KL potential. In the case of peripheral collisions (right panels of Figs. 8 and 9) we observe that the calculations without potential and with the KL potential produce an equally good description of the data, while the BR potential leads to a slight underestimation of the kaon yield.

C. Collective flows

Extraction of collective flows requires a knowledge of a reaction plane, i.e. the plane which is parallel to the impact parameter and to the beam momentum [56]. In theoretical calculations the reaction plane is obviously known. Experimentally, however, the reaction plane is usually taken parallel to the difference of transverse momenta of charged particles — which are mostly protons at SIS energies — in the forward and backward hemispheres in the c.m. frame of colliding nuclei. Thus, a collective flow carries an information about the correlations between the particle under study and the remaining protons. This makes the collective flow observables extremely useful to constrain the mean field potentials of the particles (c.f. Refs. [5, 6, 7, 8, 9] for K and \bar{K} flows).

Fig. 10 shows a mean transverse momentum projected on the reaction plane as a function of a normalized rapidity $Y^{(0)} \equiv (y/y_{proj})_{c.m.}$ for Λ hyperons (upper panel) and for protons (lower panel) for the system Ni+Ni at 1.93 A GeV. For comparison, we have selected the FOPI data [25]. The proton flow ($\equiv d\langle p_x \rangle / dY^{(0)}$ at $Y^{(0)} = 0$) is quite well described. In the calculation of the Λ flow we have taken into account both Λ 's and Σ^0 's, since in the data [25] both kinds of the Λ hyperons, those primary and those originating from $\Sigma^0 \rightarrow \Lambda + \gamma$ decays, are indistinguishable. For simplicity, we have neglected, however, a difference between the momenta of the decaying Σ^0 and the outgoing Λ . A correction for a recoil momentum due to the photon emission should slightly reduce the calculated flow. Nevertheless, we observe a rather good agreement with the data on the Λ -flow. This supports our choice of the hyperon mean field (see Sect. II).

It was shown in Ref. [11] that the FOPI data [18] on the K^+ in-plane flow can be reasonably well described using the BR parametrization of the kaon potential. Before discussing an out-of-plane flow, we will also compare our calculations with the FOPI data [18, 27] on the K^+ in-plane flow.

Fig. 11 shows the K^+ in-plane flow for Ni+Ni collisions at 1.93 A GeV in comparison to the data from Ref. [18]. In full agreement with earlier calculations of Ref. [11] we observe that the BR parametrization describes the data best (the solid line with open circles). The KL parametrization (dotted line with open squares) does not give an enough repulsion to get the negative flow. Neglecting the space component \mathbf{V} of the kaon vector field in both calculations, i.e. using static potentials, results in too negative flow for both the BR (solid

line with open pentagons) and the KL (dotted line with open diamonds) parametrizations. This was also pointed out earlier in [11]. The compensation of the repulsive static potential by the \mathbf{V} field is so strong, that, e.g. the KL parametrization gives practically the same (positive) flow as the calculation without kaon potential (dashed line with open triangles) !

An azimuthal distribution with respect to the reaction plane can be represented by a Fourier expansion :

$$\frac{dN}{d\phi}(\phi) \propto 1 + \sum_{n=1}^{\infty} 2v_n \cos(n\phi) . \quad (8)$$

The first two coefficients, v_1 and v_2 , in Eq.(8) are called directed and elliptic flow, respectively, and are expressed as follows :

$$v_1 = \langle \cos \phi \rangle = \langle p_x/p_t \rangle \quad (9)$$

$$v_2 = \langle \cos(2\phi) \rangle = \langle (p_x^2 - p_y^2)/p_t^2 \rangle . \quad (10)$$

By neglecting the terms with $n \geq 4$ in (8), the elliptic flow can be related to a ratio of particle numbers emitted out ($\phi = \pm 90^\circ$) and in ($\phi = 0^\circ$ and 180°) the reaction plane :

$$R = \frac{dN/d\phi(90^\circ) + dN/d\phi(-90^\circ)}{dN/d\phi(0^\circ) + dN/d\phi(180^\circ)} \simeq \frac{1 - 2v_2}{1 + 2v_2} . \quad (11)$$

Fig. 12 shows the directed flow v_1 as a function of the transverse momentum p_t for protons around the target rapidity from semicentral Ni+Ni collisions at 1.93 A GeV. We, first, considered all the protons including those bound in the target spectator remnant (dashed line with open circles). Then we selected only the protons separated from other particles by a critical distance $d_c > 3$ fm (solid line with open squares). The proton directed flow is negative in agreement with Fig. 10. We observe a sensitivity of v_1 at low p_t 's to the selection of protons: the calculation including only the separated protons gives a somewhat smaller absolute value of v_1 than the calculation including all protons. The directed flow at large p_t 's is independent of the proton selection procedure, and we fail to describe the data here. We ascribe this problem to a too hard momentum dependence of the nucleon mean field at large momenta [41], which pushes the high-momentum protons too early from the system, before the directed flow develops. We do not expect, however, that this drawback influences kaon propagation, since the high- p_t nucleons are not abundant and their contribution to the kaon mean field is small.

Fig. 13 displays the directed flow of kaons near target rapidity as a function of p_t for the semicentral collisions Ni+Ni at 1.93 A GeV. In the upper panel of Fig. 13 we present by solid

lines the calculations employing the BR parametrization (open circles — full calculation, open pentagons — without \mathbf{V} field) and by dotted lines — the calculations employing the KL parametrization (open squares — full calculation, open diamonds — without \mathbf{V} field). One can see, that the v_1 coefficient of K^+ 's is very sensitive to the choice of the kaon potential. As in the case of $\langle p_x \rangle$ vs $Y^{(0)}$ (c.f. Fig. 11), the BR parametrization provides the best description of the data. The KL parametrization gives a too small value of v_1 indicating not enough repulsion. Neglecting the \mathbf{V} field results in too large values of v_1 for the both parametrizations.

In the lower panel of Fig. 13 we explore the relative importance of the kaon-nucleon (KN) scattering and of the kaon potential for the description of the directed flow. To this aim, we have performed three additional calculations: (i) keeping the BR kaon mean field, but without the KN scattering (solid line with open down triangles), (ii) without kaon mean field, but with the KN scattering (dashed line with open up triangles), and (iii) without kaon mean field and without the KN scattering (dash-dotted line with stars). We see that without the kaon mean field it is impossible to reproduce the measured positive v_1 at small transverse momenta. The v_1 vs p_t dependence for kaons is similar to the one for protons (c.f. Fig. 12) in this case. The kaon mean field alone gives already the correct value of v_1 . The KN scattering reduces v_1 slightly. This is expected, since the KN collisions should make kaons to “flow” together with nucleons.

Figs. 14, 15 and 16 show the azimuthal distributions of K^+ 's at midrapidity from semi-central collisions Ni+Ni at 1.93 A GeV, Au+Au at 1 A GeV and Au+Au at 1.5 A GeV, respectively, in comparison to the data from Refs. [24, 29]. In order to quantify an anisotropy of the azimuthal distributions we have performed a fit of these distributions as in Refs. [24, 29] :

$$\frac{dN}{d\phi}(\phi) \propto 1 + 2v_1 \cos(\phi) + 2v_2 \cos(2\phi) . \quad (12)$$

The elliptic flows v_2 for the data and for different calculations are collected in the Table II [57].

The experimental data for all three systems reveal a pronounced out-of-plane ($v_2 < 0$) emission of K^+ 's. Overall, the calculations with the BR parametrization of the kaon mean field (solid lines with open circles) provide the most reasonable description of the data on the azimuthal distributions. The calculations with the KL parametrization (dotted lines with open boxes) produce not enough anisotropy.

In order to understand the mechanism of the out-of-plane K^+ enhancement better, we have performed additional calculations by switching-off various effects. The calculations without the space component of the kaon vector field \mathbf{V} (solid lines with open pentagons for the BR parametrization and dotted lines with open diamonds for the KL one) differ only very slightly from the full calculations, contrary to the findings of Ref. [23] on the influence of the Lorentz force on the kaon squeeze-out. We recall, that for the in-plane flow (c.f. Figs. (11),(13)) there is a strong influence of the \mathbf{V} field, in agreement with the results of Ref. [11].

The squeeze-out of particles can be caused either by a dynamical focusing due to a repulsive mean field [58] or by a shadowing of in-plane emitted particles by spectator pieces [41]. Shadowing implies a dominant role of scattering and/or absorption of the particles on nucleons. What determines the kaon squeeze-out: the kaon mean field or the KN scattering? To answer this question, as in the case of the directed flow, we present in the lower panels of Figs. 14,15,16 the results (i) with the BR parametrization, but without the KN scattering, (ii) without kaon mean field, but with the KN scattering, and (iii) without kaon mean field and without the KN scattering. (the meaning of the lines is the same as in the lower panel of Fig. 13 discussed above). In the calculation (iii) there is no squeeze-out signal. The calculations (i) and (ii) both produce the squeeze-out. However, in the first case the signal is stronger than in the second case. Furthermore, the calculation (i) gives almost the same azimuthal distribution and the elliptic flow v_2 as the full calculation including the BR parametrization and the KN scattering. In the case (i) the mechanism of the out-of-plane enhancement can be only the dynamical focusing, while in the case (ii) only the shadowing is active. Thus, in our calculations the squeeze-out of K^+ 's is caused mainly by the mechanism of the dynamical focusing by the repulsive mean field.

For comparison with kaons we, finally, present in Fig. 17 the azimuthal distributions of the π^+ 's at midrapidity from the semicentral collisions Au+Au at 1.5 A GeV and Ni+Ni at 1.93 A GeV. The corresponding elliptic flows v_2 — obtained in a similar fit procedure as discussed above in the case of kaons — are given in the Table III. Since a pion potential is not included in our calculations, we can not expect a good agreement with the data [29]. Indeed, in the case of Au+Au at 1.5 A GeV we underestimate the measured squeeze-out signal. The same result was observed earlier in Ref. [42] for the case of Au+Au at 1 A GeV. For the lighter system and higher energy (Ni+Ni at 1.93 A GeV) the influence of the pion

mean field should be smaller and here our calculation is able to reproduce the data [29].

IV. SUMMARY AND DISCUSSION

We have studied the K^+ production and propagation in heavy-ion collisions at the SIS energies on the basis of the BUU model [30, 31, 32]. The model propagates explicitly a large set of the N^* and Δ resonances and includes the two main kaon production channels which are relevant ones at the beam energies of 1-2 A GeV : $BB \rightarrow BYK$ and $\pi B \rightarrow KY$. The potentials of a nonstrange baryon B , of a hyperon Y and (optionally) of a kaon K were included in the cross sections via shifts of the thresholds. For the kaon potential we have used the BR and the KL parametrizations, which have been already applied in Ref. [11]. The KL parametrization can be derived from the lowest-order approximation to the chiral Lagrangian [6]. The BR parametrization [19], in distinction to the KL one, takes into account the in-medium pion decay constant in the kaon vector field and also has a larger kaon-nucleon sigma term.

First, we have looked at the K^+ yields and spectra. The secondary processes $RN \rightarrow BYK$ and $\pi B \rightarrow KY$ have a big contribution to the kaon production (see the Table I and Fig. 4c). This makes the kaon yield very sensitive to the in-medium reduction of the $NN \leftrightarrow NR$ cross sections. In our “standard” calculation, which includes the SM nucleon mean field, the in-medium $NN \leftrightarrow NR$ cross sections [32] and the kaon mean field in the BR parametrization, we have obtained a very good description of the kaon multiplicities for both heavy and light colliding systems in all the SIS energy region, in agreement with the QMD calculations of Ref. [3]. For a light system C+C at 2 A GeV the p_{lab} -spectra are reproduced quite well, which is also shown in Ref. [11]. However, for heavy systems Au+Au and Ni+Ni the calculated p_{lab} -, E_{kin}^{cm} - and m_T -spectra are somewhat too hard. The repulsive kaon potential reduces the yield of soft kaons and leaves the yield of hard kaons practically unchanged. Thus, the kaon potential makes the kaon spectra harder. In most cases the slopes of the K^+ spectra are reasonably well described by the calculation without kaon potential. But this calculation drastically overestimates the kaon multiplicity. Moreover, the slopes of the E_{kin}^{cm} -spectra for the central collisions of the heaviest system Au+Au at 1.5 A GeV can be *only* described by using the repulsive kaon potential (Fig. 7).

Second, we have studied the collective in-plane and out-of-plane flows of K^+ 's. The $\langle p_x \rangle$

vs $Y^{(0)}$ and v_1 vs p_t dependencies for kaons emitted from semicentral Ni+Ni collisions at 1.93 A GeV are very sensitive to the choice of the kaon mean field and clearly favour the BR parametrization, as was also recently shown in Ref. [11]. The azimuthal distributions of kaons at midrapidity are also sensitive to the choice of the kaon mean field. The KN scattering alone gives a too weak squeeze-out signal with respect to the data. For the heaviest measured system Au+Au at 1 and 1.5 A GeV, the data on the elliptic flow v_2 are best described by using the BR parametrization. For a lighter system Ni+Ni at 1.93 A GeV the calculation with the KL parametrization reproduces the data on v_2 best, but the BR one is also consistent with the data within the experimental errorbars.

The Lorentz force caused by the space components \mathbf{V} of the kaon vector field does not significantly influence the azimuthal distributions of kaons at the midrapidity. However, in the case of the in-plane flow the Lorentz force is found to contribute very strongly [11] (see also our Figs. 11,13). Thus, the kaon azimuthal distributions at midrapidity probe, basically, the static kaon potential.

Some comments are also in order with regard to our results of a recent benchmark test of the transport codes [38]. Our results in [38] were obtained with an enforced $\Delta(1232)$ lifetime of $\hbar/120$ MeV and with the vacuum $NN \leftrightarrow NR$ cross sections. In our standard calculations, however, we use the $\Delta(1232)$ lifetime of $\hbar/\Gamma_\Delta(M)$, where $\Gamma_\Delta(M)$ is the mass dependent width of the $\Delta(1232)$ -resonance [30], and the in-medium $NN \leftrightarrow NR$ cross sections. In particular, using the vacuum $NN \leftrightarrow NR$ cross sections in [38] has led to enhanced pion and kaon yields in our calculations with respect to most other transport calculations. However, our results [38] on π^\pm 's and K^+ 's agree with those obtained with the BUU code of Refs. [59, 60, 61], which also propagates explicitly a large set of the baryonic resonances with $M < 2$ GeV. Thus, our present study demonstrates clearly, that the effect of the higher baryonic resonances on the pion and kaon production is counterbalanced by the in-medium reduction of the $NN \leftrightarrow NR$ cross sections, which produces a satisfactory agreement with experimental data.

In conclusion, the BR parametrization of the kaon mean field provides the best overall description of the K^+ observables at SIS energies. The remaining problem lies in the somewhat too hard p_{lab} -spectra for the Au+Au collisions. These spectra, however, are sensitive not only to the choice of the kaon mean field, but also to the kaon production cross sections in nuclear medium, which are still rather ambiguous. The in-medium calculation for the

channel $\pi B \rightarrow YK$ has been performed in Ref. [62] indicating a reduction of the cross section at a finite baryon density. Such an in-medium calculation is still needed, however, for another important channel $BB \rightarrow BYK$, basing e.g. on the model of Ref. [43].

Acknowledgments

We gratefully acknowledge support by the Frankfurt Center for Scientific Computing.

-
- [1] J. Randrup and C.M. Ko, Nucl. Phys. A **343**, 519 (1980).
 - [2] J. Aichelin and C.M. Ko, Phys. Rev. Lett. **55**, 2661 (1985).
 - [3] C. Fuchs, Amand Faessler, E. Zabrodin, Yu-Ming Zheng, Phys. Rev. Lett. **86**, 1974 (2001).
 - [4] C. Sturm et al., KaoS Collaboration, Phys. Rev. Lett. **86**, 39 (2001).
 - [5] G.Q. Li, C.M. Ko, and Bao-An Li, Phys. Rev. Lett. **74**, 235 (1995).
 - [6] G.Q. Li, C.M. Ko, Nucl. Phys. A **594**, 460 (1995).
 - [7] G.Q. Li et al., Phys. Lett. B **381**, 17 (1996).
 - [8] G.Q. Li and C.M. Ko, Phys. Rev. C **54**, R2159 (1996).
 - [9] E.L. Bratkovskaya, W. Cassing, U. Mosel, Nucl. Phys. A **622**, 593 (1997).
 - [10] C. David, C. Hartnack and J. Aichelin, Nucl. Phys. A **650**, 358 (1999).
 - [11] Yu-Ming Zheng, C. Fuchs, Amand Faessler, K. Shekhter, Yu-Peng Yan, Chinorat Kobdaj, Phys. Rev. C **69**, 034907 (2004).
 - [12] A. Mishra, E.L. Bratkovskaya, J. Schaffner-Bielich, S. Schramm, H. Stoecker, Phys. Rev. C **70**, 044904 (2004).
 - [13] D.B. Kaplan and A.E. Nelson, Phys. Lett. B **175**, 57 (1986).
 - [14] A.E. Nelson and D.B. Kaplan, Phys. Lett. B **192**, 193 (1987).
 - [15] N. Herrmann et al., FOPI Collaboration, Nucl. Phys. A **610**, 49c (1996).
 - [16] Z. Rudy, W. Cassing, L. Jarczyk, B. Kamys, A. Kowalczyk, and P. Kulessa, Eur. Phys. J. A **23**, 379 (2005).
 - [17] C. Fuchs, D.S. Kosov, Amand Faessler, Z.S. Wang, T. Waizdych, Phys. Lett. B **434**, 245 (1998).
 - [18] N. Herrmann et al., FOPI Collaboration, Prog. Part. Nucl. Phys. **42**, 187 (1999).
 - [19] G.E. Brown and M. Rho, Nucl. Phys. A **596**, 503 (1996).
 - [20] Jürgen Schaffner-Bielich, Igor N. Mishustin, Jakob Bondorf, Nucl. Phys. A **625**, 325 (1997).
 - [21] C.L. Korpa and M.F.M. Lutz, Acta Phys. Hung. A**22**, 21 (2005), nucl-th/0404088.
 - [22] Laura Tolós, Angels Ramos, Artur Polls, hep-ph/0503009.
 - [23] Z.S. Wang, C. Fuchs, A. Faessler, T. Gross-Boelting, Eur. Phys. J. A **5**, 275 (1999).
 - [24] Y. Shin et al., KaoS Collaboration, Phys. Rev. Lett. **81**, 1576 (1998).
 - [25] J.L. Ritman et al, FOPI Collaboration, Z. Phys. A **352**, 355 (1995).

- [26] M. Menzel et al., KaoS Collaboration, Phys. Lett. B **495**, 26 (2000).
- [27] P. Crochet et al., FOPI Collaboration, Phys. Lett. B **486**, 6 (2000).
- [28] A. Förster et al., KaoS Collaboration, Phys. Rev. Lett. **91**, 152301 (2003).
- [29] F. Uhlig et al., KaoS Collaboration, nucl-ex/0411021.
- [30] M. Effenberger, E.L. Bratkovskaya, and U. Mosel, Phys. Rev. C **60**, 44614 (1999).
- [31] M. Effenberger, PhD thesis, Uni. Giessen, 1999,
<http://theorie.physik.uni-giessen.de/html/dissertations.html>.
- [32] A.B. Larionov and U. Mosel, Nucl. Phys. A **728**, 135 (2003).
- [33] C. Hartnack, H. Oeschler and J. Aichelin, Phys. Rev. Lett. **90**, 102302 (2003).
- [34] C. Hartnack and J. Aichelin, J. Phys. G **30**, S531 (2004).
- [35] J. Aichelin, Phys. Rep. **202**, 233 (1991).
- [36] C. Hartnack, Rajeev K. Puri, J. Aichelin, J. Konopka, S.A. Bass, H. Stoecker, W. Greiner,
Eur. Phys. J. A **1**, 151 (1998).
- [37] W. Cassing and E.L. Bratkovskaya, Phys. Rep. **308**, 65 (1999).
- [38] E.E. Kolomeitsev et al., nucl-th/0412037.
- [39] D.M. Manley and E.M. Saleski, Phys. Rev. D **45**, 4002 (1992).
- [40] J. Lehr, M. Effenberger, U. Mosel, Nucl. Phys. A **671**, 503 (2000).
- [41] A.B. Larionov, W. Cassing, C. Greiner, U. Mosel, Phys. Rev. C **62**, 064611 (2000).
- [42] A.B. Larionov, W. Cassing, S. Leupold, and U. Mosel, Nucl. Phys. A **696**, 747 (2001).
- [43] K. Tsushima, A. Sibirtsev, A.W. Thomas, G.Q. Li, Phys. Rev. C **59**, 369 (1999).
- [44] W. Cassing, E.L. Bratkovskaya, U. Mosel, S. Teis, and A. Sibirtsev, Nucl. Phys. A **614**, 415
(1997).
- [45] K. Tsushima, S.W. Huang, and A. Faessler, Austral. J. Phys. **50**, 35 (1997).
- [46] A. Sibirtsev, W. Cassing, and C.M. Ko, Z. Phys. A **358**, 101 (1997).
- [47] A. Baldini et al., Landolt-Börnstein, V. 12, Springer Verlag, Berlin, 1987.
- [48] X.S. Fang, C.M. Ko, G.Q. Li, and Y.M. Zheng, Phys. Rev. C **49**, R608 (1994).
- [49] S.J. Lee, J. Fink, A.B. Balantekin, M.R. Strayer, A.S. Umar, P.-G. Reinhard, J.A. Maruhn,
W. Greiner, Phys. Rev. Lett. **57**, 2916 (1986).
- [50] Please, do not mix these masses with the Dirac masses !
- [51] G.Q. Li, C.-H. Lee, G.E. Brown, Nucl. Phys. A **625**, 372 (1997).
- [52] C. Sturm, thesis, TU Darmstadt, 2001.

- [53] Notice, that in Fig. 2a and in Table I we have summed up both channels nucleon- $\Delta(1232)$ and nucleon-higher resonance, while in Fig. 4c these channels are shown separately.
- [54] A.B. Larionov and U. Mosel, Phys. Rev. C **66**, 034902 (2002).
- [55] To avoid misunderstanding, we would like to recall that the *total* K^+ multiplicity is presented in the lower panel of Fig. 7, while the K^+ spectra on Fig. 6 are taken at $\Theta_{lab} = 40^\circ$.
- [56] P. Danielewicz, G. Odyniec, Phys. Lett. B **157**, 146 (1985).
- [57] The parameters v_1 and v_2 of the fit (12) are equal to those given by Eqs.(9),(10) within accuracy up to the terms with $n > 2$ in the Fourier expansion (8), which we neglect. Thus, we will also call the fit parameters v_1 and v_2 as the directed and elliptic flows, respectively. Since the azimuthal distributions are extracted at midrapidity, the directed flow v_1 should be equal to zero due to symmetry reasons. We have obtained $v_1 \sim 10^{-3}$ in the fitting procedure due to a finite statistics, which is much smaller than the extracted values of $|v_2|$. Thus, we drop the explicit values of the v_1 coefficient.
- [58] P. Danielewicz, Nucl. Phys. A **673**, 375 (2000).
- [59] Gy. Wolf, W. Cassing, and U. Mosel, Nucl. Phys. A **552**, 549 (1993).
- [60] Gy. Wolf, Heavy Ion Physics **5**, 281 (1997).
- [61] H.W. Barz and L. Naumann, Phys. Rev. C **68**, 041901R (2003).
- [62] K. Tsushima, A. Sibirtsev, and A.W. Thomas, Phys. Rev. C **62**, 064904 (2000).

TABLE I: Contribution of the different kaon production channels to the total kaon number from central ($b = 0$ fm) collisions of the various systems.

Channel	Au+Au, 0.96 A GeV	Au+Au, 1.48 A GeV	Ni+Ni, 1.93 A GeV
$RN \rightarrow BYK$	51%	47%	36%
$NN \rightarrow BYK$	12%	25%	47%
$\pi B \rightarrow KY$	25%	17%	10%
$RR \rightarrow BYK$	8%	6%	3%
$\pi B \rightarrow K\bar{K}N$	3%	3%	2%
$BB \rightarrow NNK\bar{K}$	1%	2%	2%

TABLE II: The elliptic flow v_2 obtained by the fit of the K^+ azimuthal distributions by a function $\propto 1 + 2v_1 \cos(\phi) + 2v_2 \cos(2\phi)$. The data are from Refs. [24, 29].

	Au+Au, 1 A GeV	Au+Au, 1.5 A GeV	Ni+Ni, 1.93 A GeV
Exp.	-0.110 ± 0.011	-0.08 ± 0.02	-0.04 ± 0.02
BR	-0.100 ± 0.007	-0.082 ± 0.004	-0.059 ± 0.002
BR w/o \mathbf{V}	-0.092 ± 0.005	-0.098 ± 0.006	-0.076 ± 0.001
BR w/o KN scatt.	-0.088 ± 0.011	-0.068 ± 0.006	-0.061 ± 0.003
KL	-0.055 ± 0.005	-0.062 ± 0.003	-0.037 ± 0.004
KL w/o \mathbf{V}	-0.080 ± 0.005	-0.062 ± 0.003	-0.041 ± 0.002
w/o pot.	-0.048 ± 0.005	-0.040 ± 0.004	-0.020 ± 0.002
w/o pot. w/o KN scatt.	-0.015 ± 0.005	-0.017 ± 0.005	-0.002 ± 0.002

TABLE III: The elliptic flow v_2 obtained by the fit of the π^+ azimuthal distributions by a function $\propto 1 + 2v_1 \cos(\phi) + 2v_2 \cos(2\phi)$. The data are from Ref. [29].

	Au+Au, 1.5 A GeV	Ni+Ni, 1.93 A GeV
Exp.	-0.15 ± 0.01	-0.04 ± 0.01
BUU	-0.063 ± 0.006	-0.041 ± 0.008

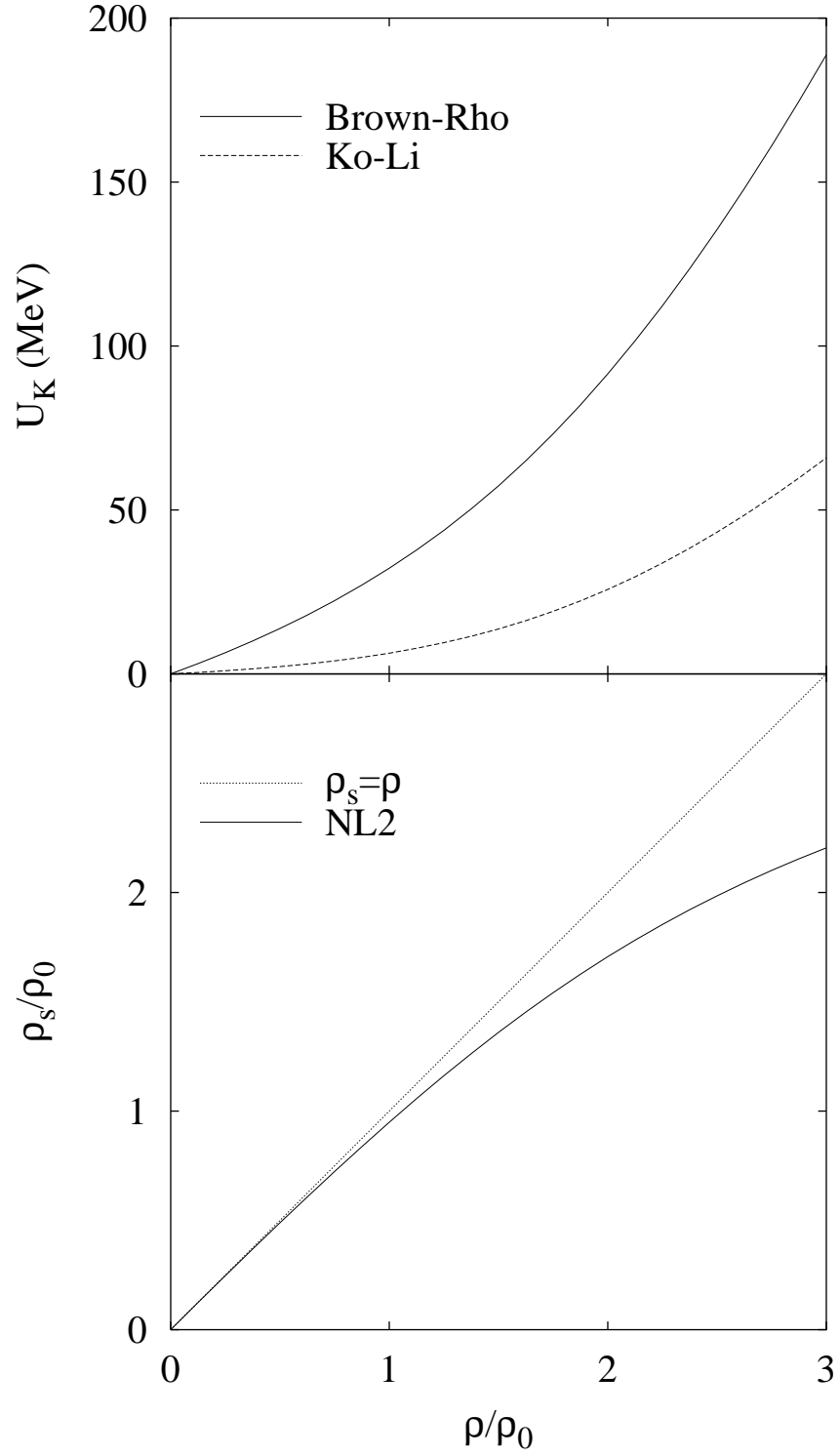


FIG. 1: Upper panel: the kaon potential at zero momentum as a function of the nuclear matter density. Lower panel: the scalar density vs the nuclear matter density.

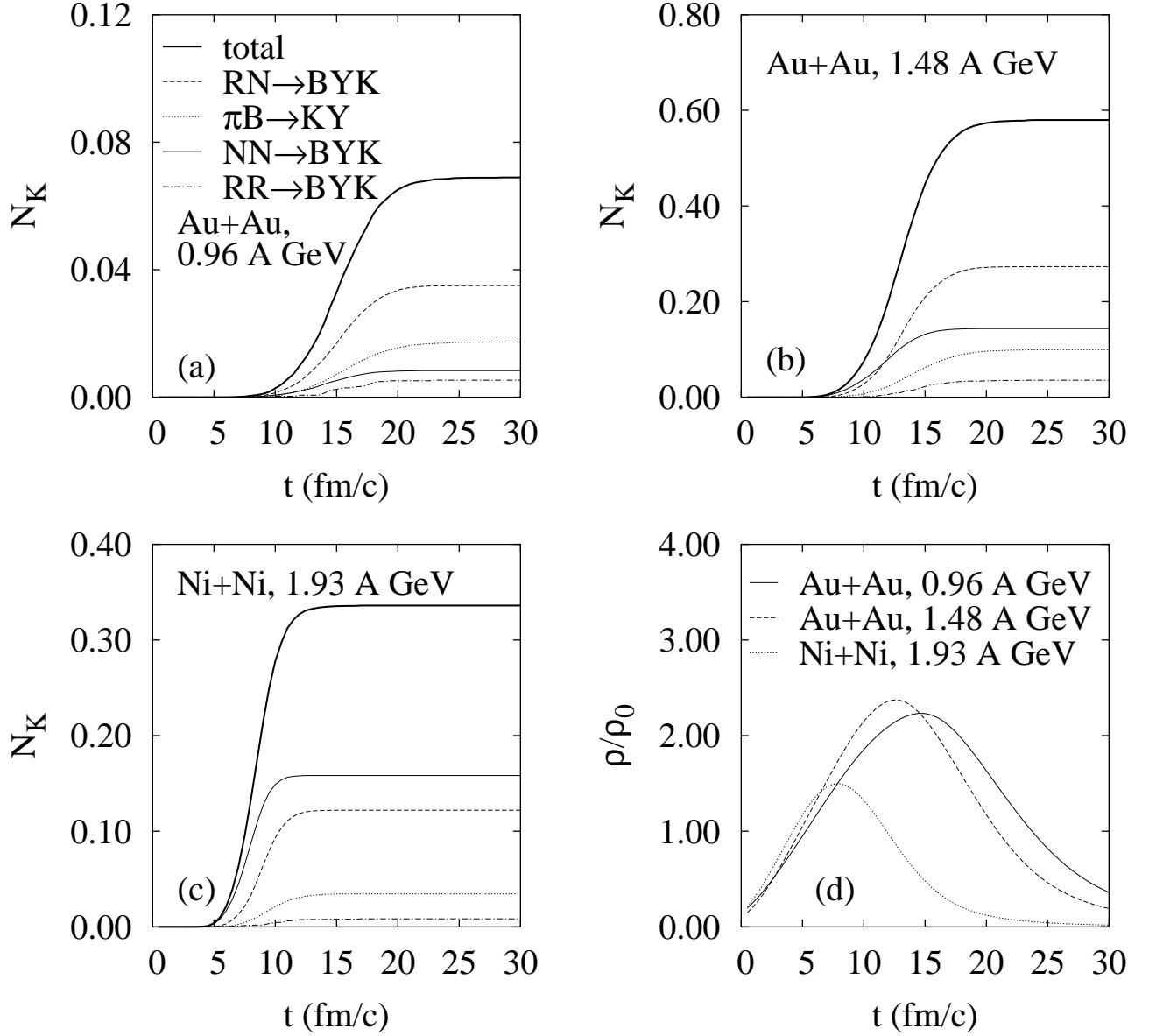


FIG. 2: Number of kaons (K^+ 's and K^0 's) as a function of time for central ($b = 0$ fm) collisions Au+Au at 0.96 A GeV (a), Au+Au at 1.48 A GeV (b) and Ni+Ni at 1.93 A GeV (c) for the different production channels: $RN \rightarrow BYK$ — dashed lines, $\pi B \rightarrow KY$ — dotted lines, $NN \rightarrow BYK$ — thin solid lines and $RR \rightarrow BYK$ — dash-dotted lines. Total kaon number is represented by thick solid lines in the panels a,b,c. Panel d shows the time evolution of a central baryon density for the central collisions Au+Au at 0.96 A GeV — solid line, Au+Au at 1.48 A GeV — dashed line and Ni+Ni at 1.93 A GeV — dotted line.

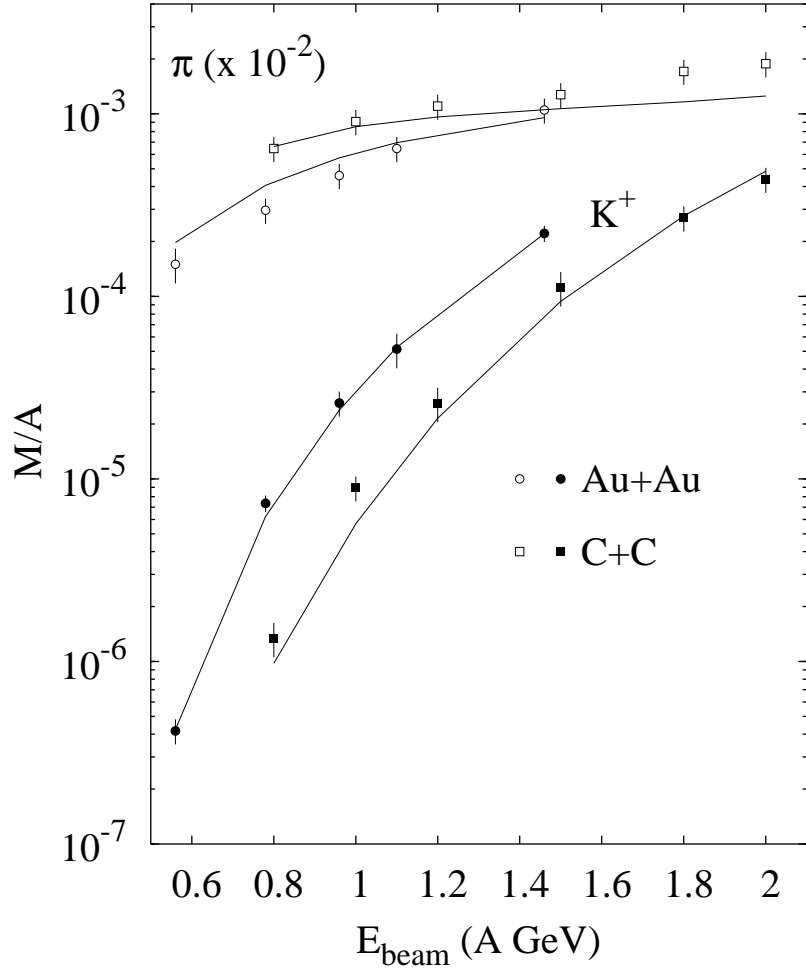


FIG. 3: Pion (upper two lines) and kaon (lower two lines) multiplicities per projectile nucleon in the C+C (highest and lowest lines) and in the Au+Au (two lines in the middle) systems vs the projectile energy. Pion multiplicity includes all pions and is scaled by a factor of 10^{-2} . Data are from Ref. [4].

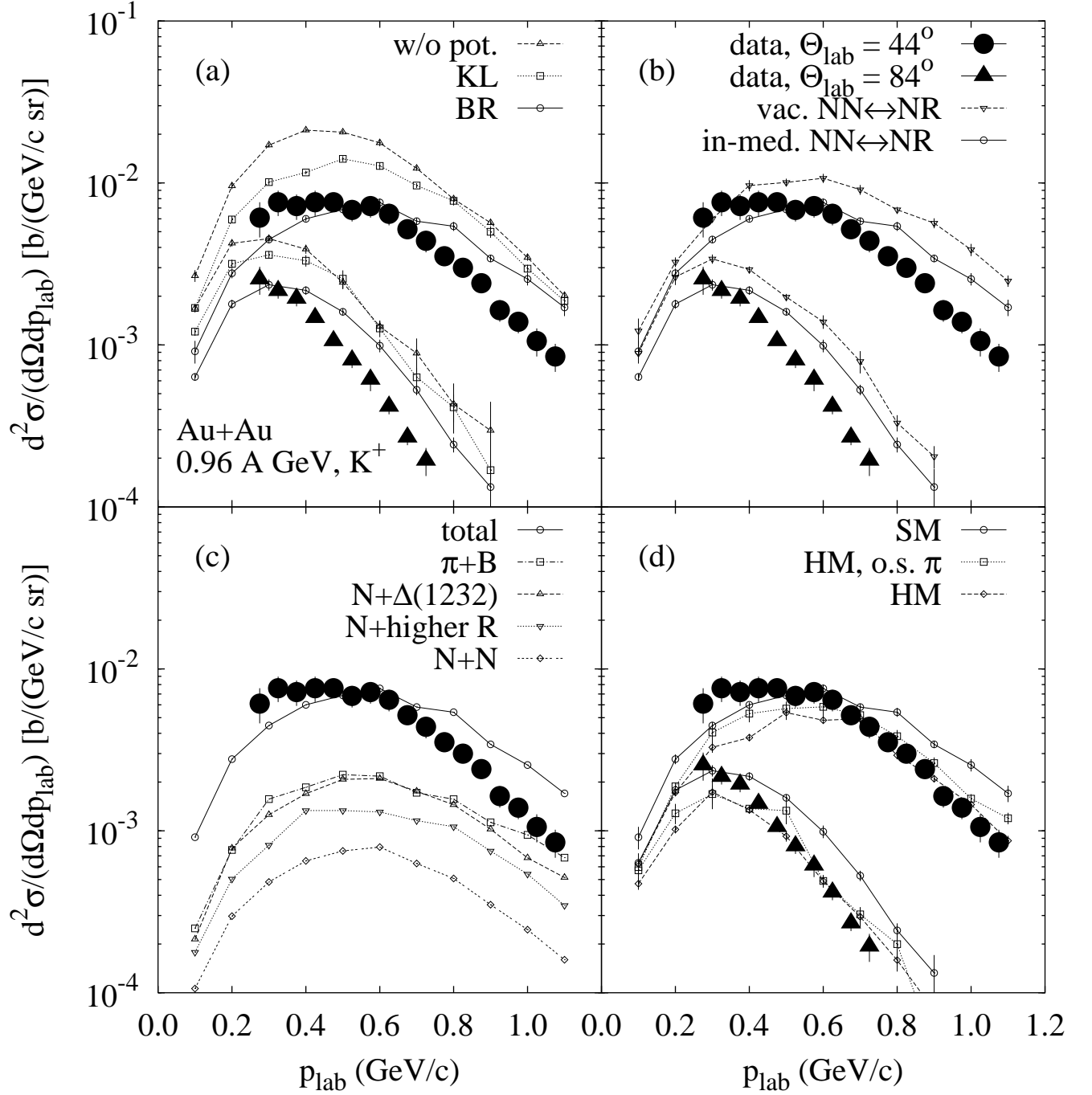


FIG. 4: Inclusive K^+ production cross section as a function of the laboratory momentum for Au+Au collisions at 0.96 A GeV at various laboratory angles. Errorbars on the calculated results are statistical. See text for further details of calculations. Data are from Ref. [4].

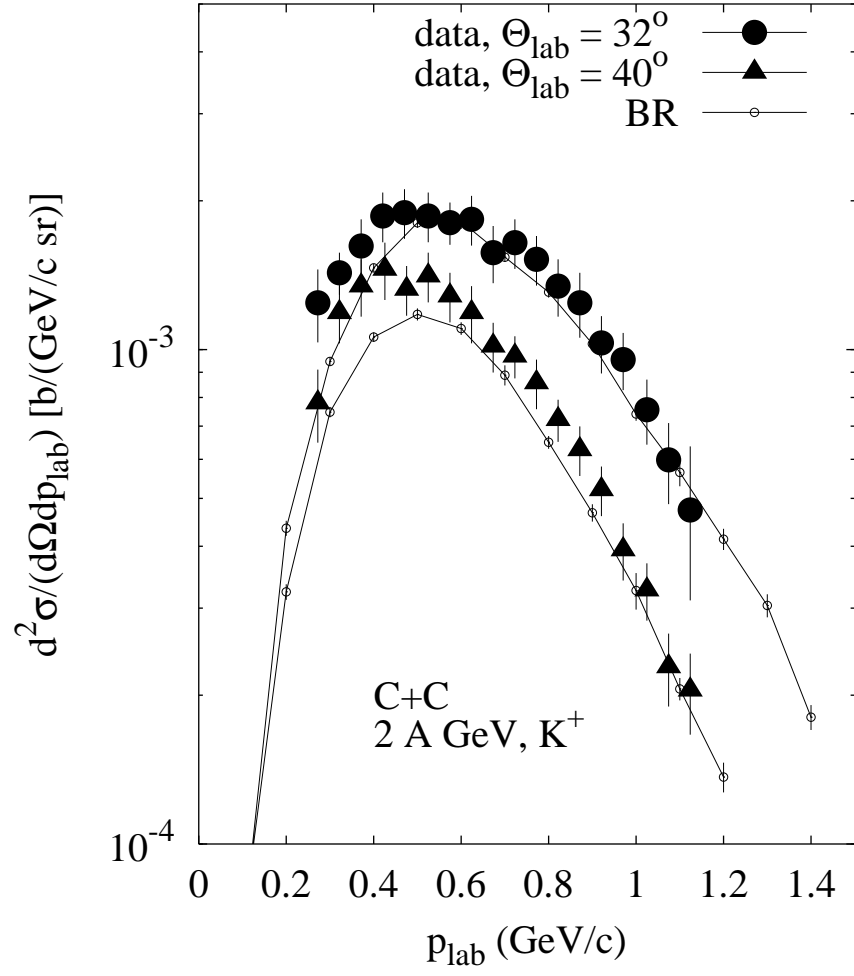


FIG. 5: Inclusive K^+ production cross section as a function of the laboratory momentum for C+C at 2 A GeV at $\Theta_{\text{lab}} = 32^\circ$ and 40° . Data are taken from Ref. [52].

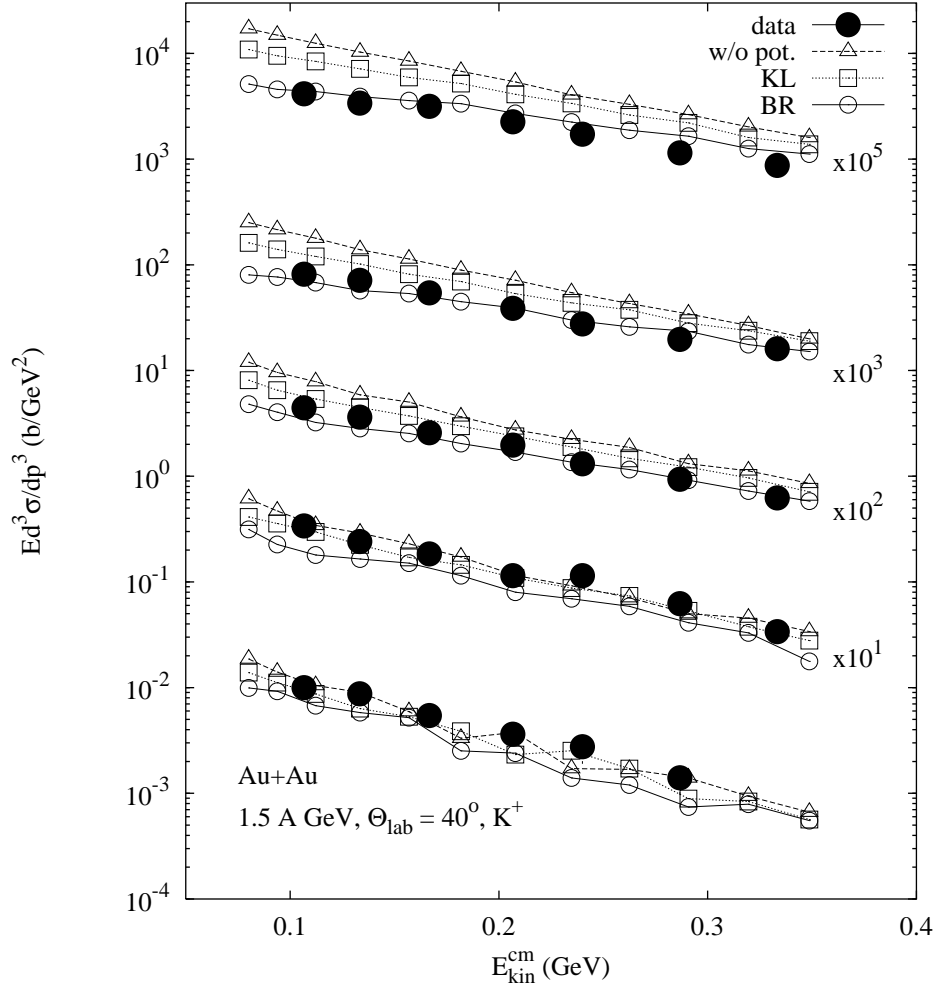


FIG. 6: Differential K^+ production cross section at $\Theta_{\text{lab}} = 40^\circ$ from Au+Au collisions at 1.5 A GeV for different centrality bins as a function of the kinetic energy in the c.m. system. Data points are taken from Ref. [28] and correspond to the following centrality bins (from top to bottom with decreasing centrality): 5%, 15%, 15%, 25% and 40% of the reaction cross section. Corresponding calculations are performed within the following impact parameter regions (from the upper to lower lines): $b \leq 3$ fm, $b = 4 - 6$ fm, $b = 7 - 8$ fm, $b = 9 - 10$ fm and $b = 11 - 14$ fm. Spectra are scaled by the factors $10^5, 10^3, 10^2, 10^1, 10^0$ from top to bottom.

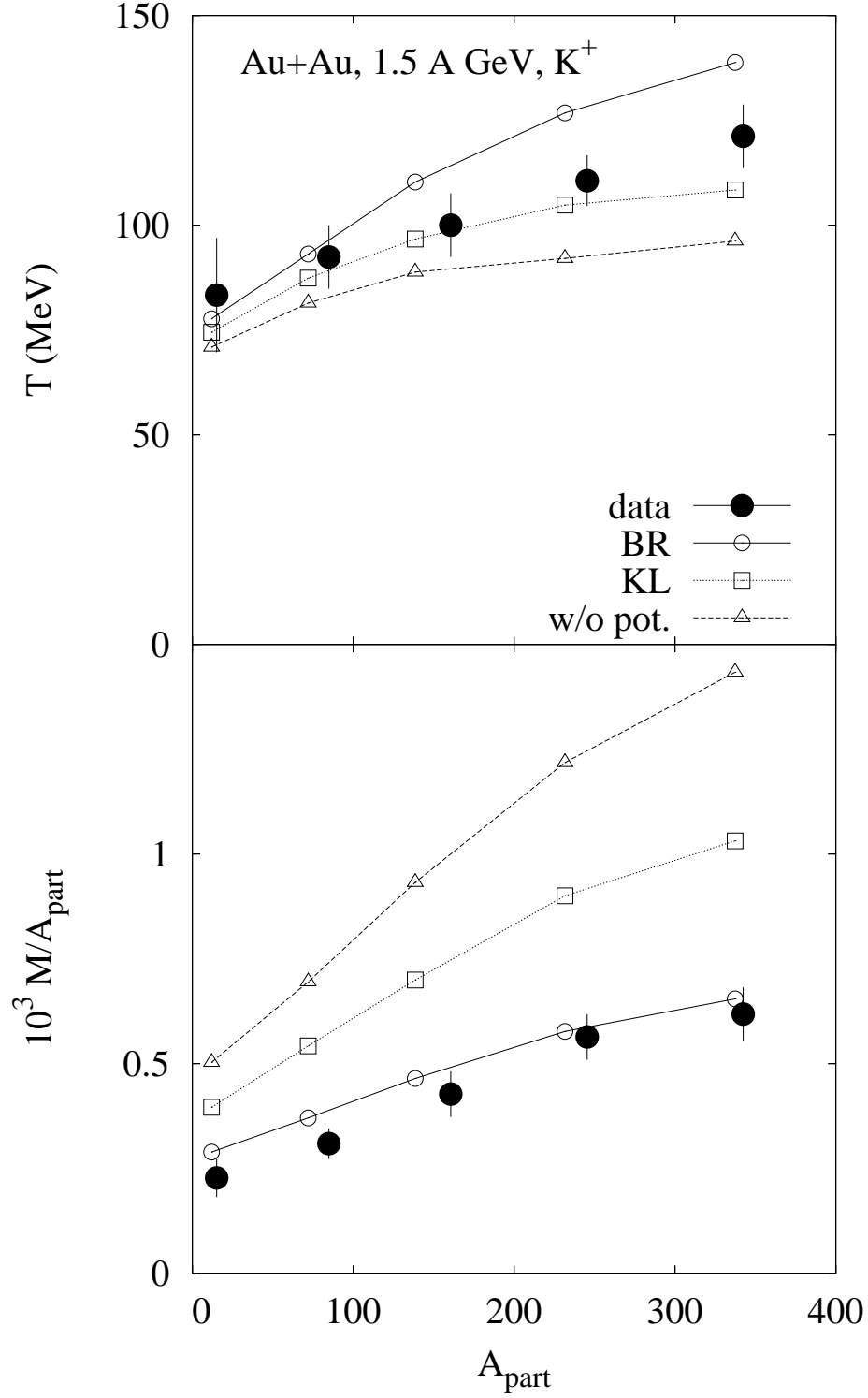


FIG. 7: Upper panel: inverse slope parameter of the K^+ c.m. kinetic energy spectrum as a function of the number of participating nucleons A_{part} for the system Au+Au at 1.5 A GeV. Lower panel: K^+ multiplicity per participating nucleon vs A_{part} for Au+Au at 1.5 A GeV. The data are from Ref. [28].

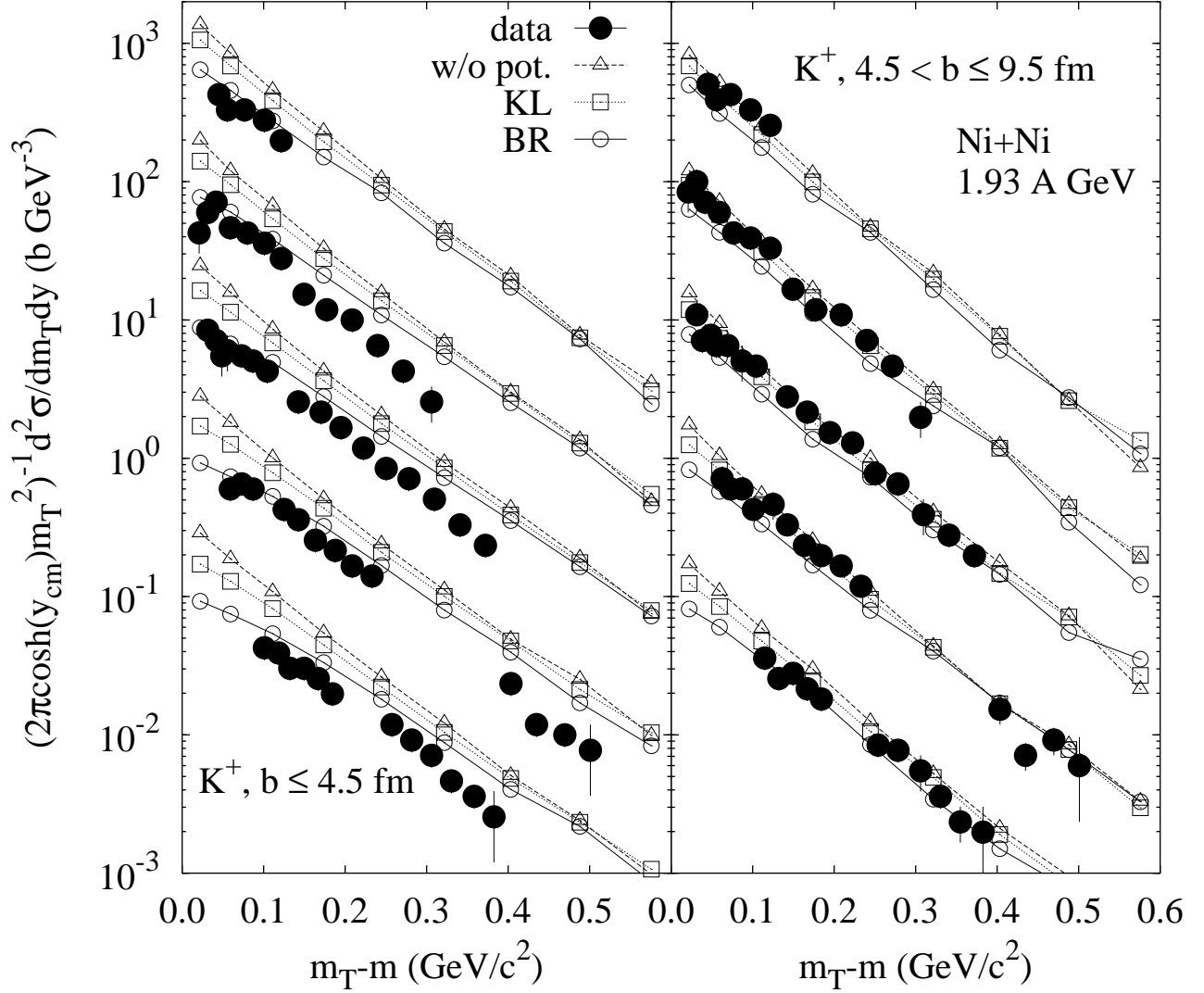


FIG. 8: Transverse mass spectra of K^+ 's from the Ni+Ni collisions at 1.93 A GeV for central events (left panel) and peripheral events (right panel) in comparison to the data from Ref. [26]. The spectra are extracted in the following c.m. rapidity intervals (from top to bottom): $-0.69 < y_{cm} < -0.54$, $-0.54 < y_{cm} < -0.39$, $-0.39 < y_{cm} < -0.24$, $-0.24 < y_{cm} < -0.09$, $-0.09 < y_{cm} < 0.06$. The scaling factors $10^4, 10^3, 10^2, 10^1$ and 10^0 are applied to the spectra from top to bottom.

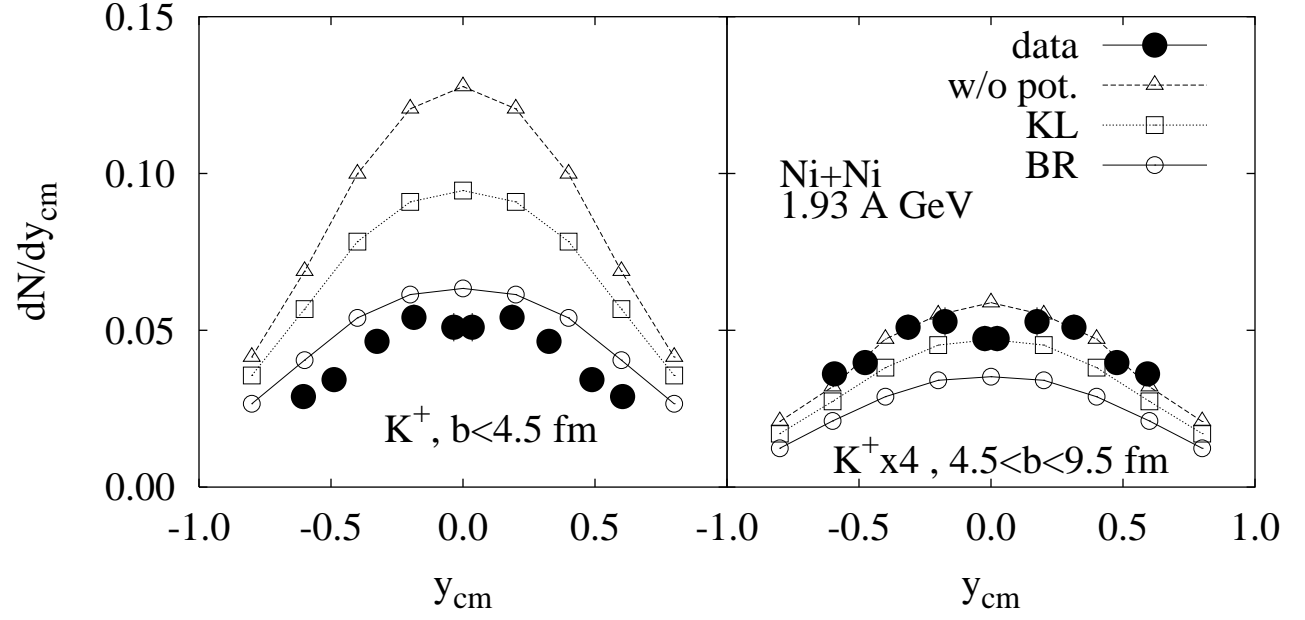


FIG. 9: K^+ c.m. rapidity distributions from the central (left panel) and peripheral (right panel) collisions of Ni+Ni at 1.93 A GeV in comparison to the the data from Ref. [26]. The distributions for the peripheral collisions are multiplied by a factor of 4.

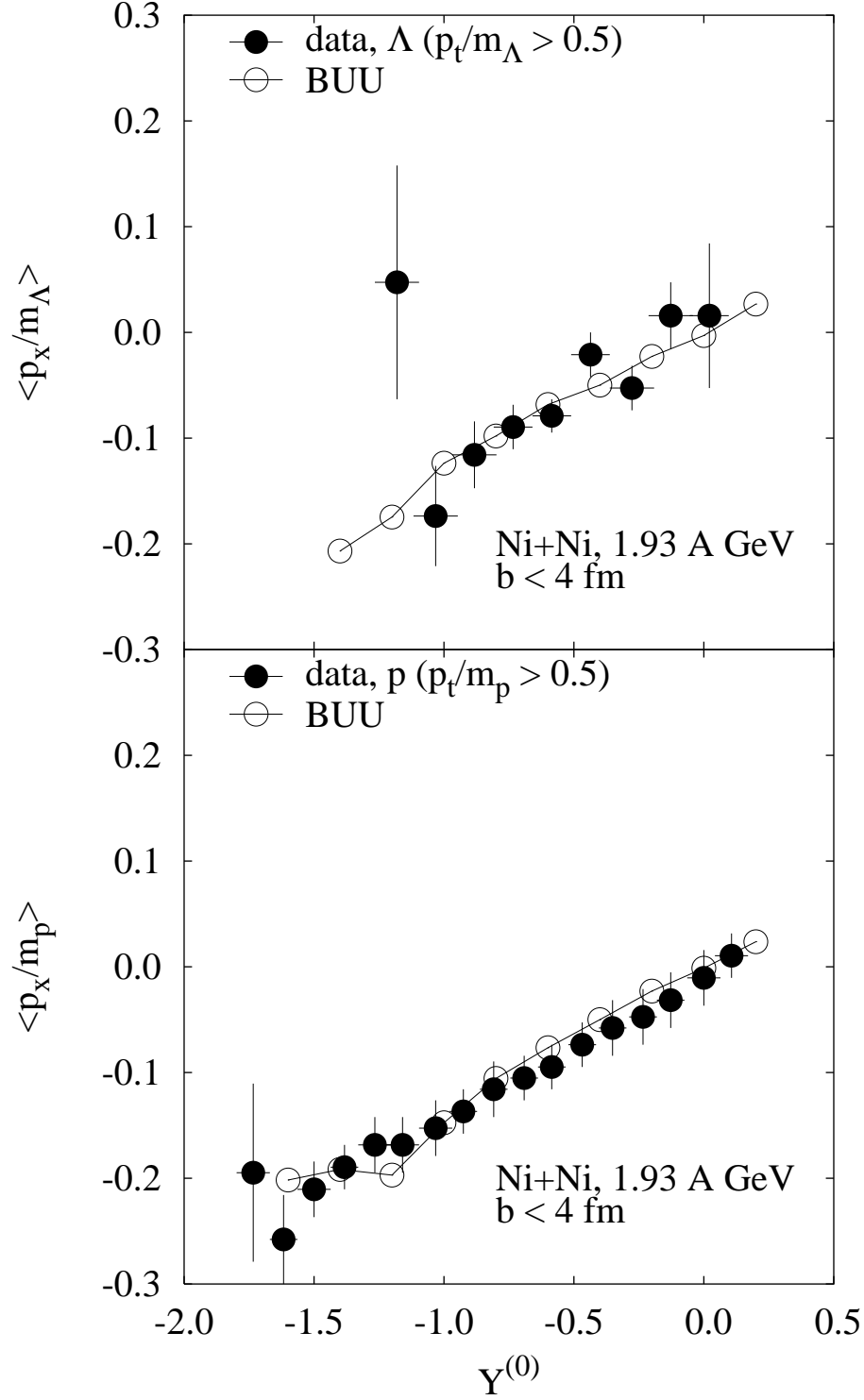


FIG. 10: Mean transverse momentum projected on the reaction plane vs the normalized rapidity for Λ hyperons (upper panel) and for protons (lower panel) for Ni+Ni collisions at 1.93 A GeV with $b < 4$ fm. The particles are selected in the transverse momentum ranges $p_t/m_\Lambda > 0.5$ for Λ 's and $p_t/m_p > 0.5$ for protons. The Central Drift Chamber (CDC) angular cuts ($30^\circ < \Theta_{lab} < 150^\circ$) are taken into account in calculations. The data are from Ref. [25].

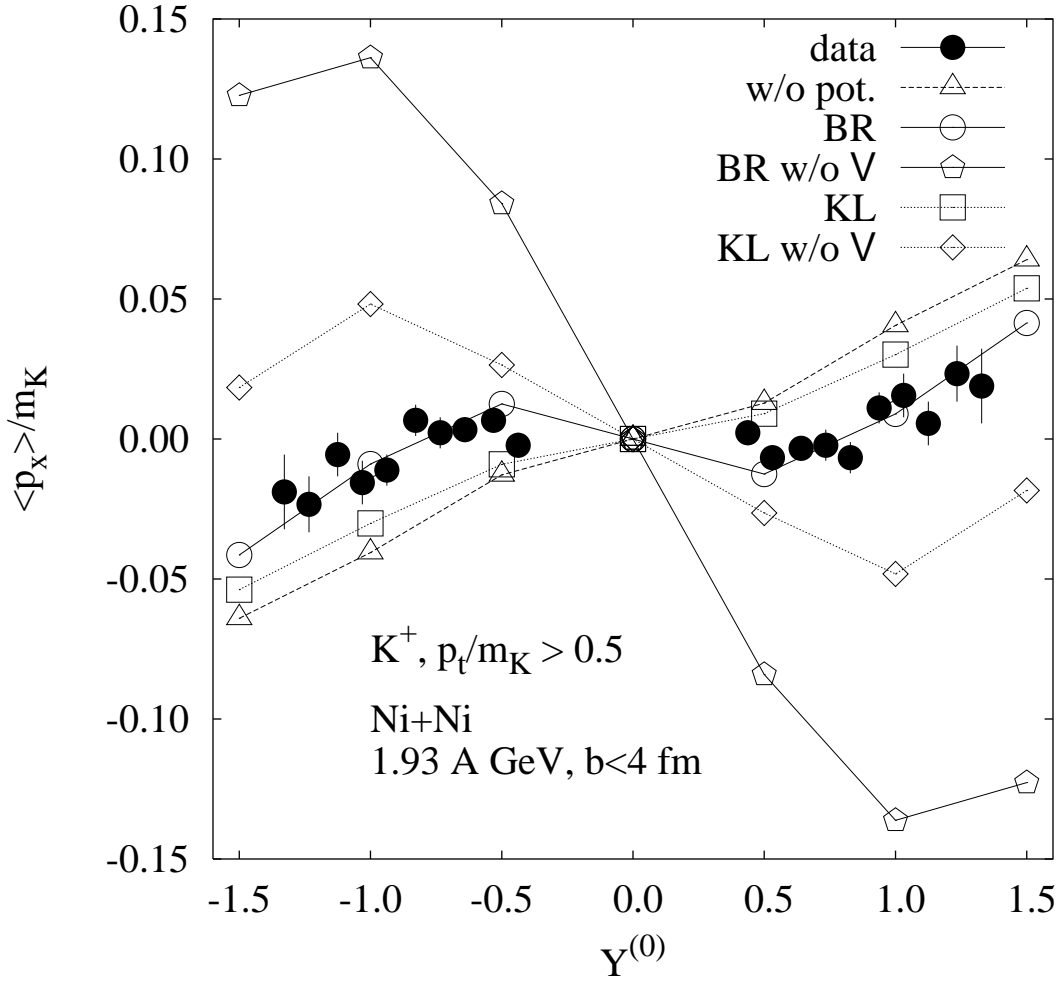


FIG. 11: K^+ mean transverse momentum projected on the reaction plane vs the normalized rapidity for Ni+Ni at 1.93 A GeV, $b < 4$ fm compared with the data from Ref. [18]. Only high transverse momentum kaons ($p_t/m_K > 0.5$) were selected according to [18]. The CDC angular cuts ($39^\circ < \Theta_{lab} < 150^\circ$) and the upper limit of the laboratory momentum (0.5 GeV/c) up to which a K^+ can be identified [18] were also taken into account in calculations. The data points and the calculated curves at $Y^{(0)} > 0$ are obtained by reflection from those at $Y^{(0)} < 0$.

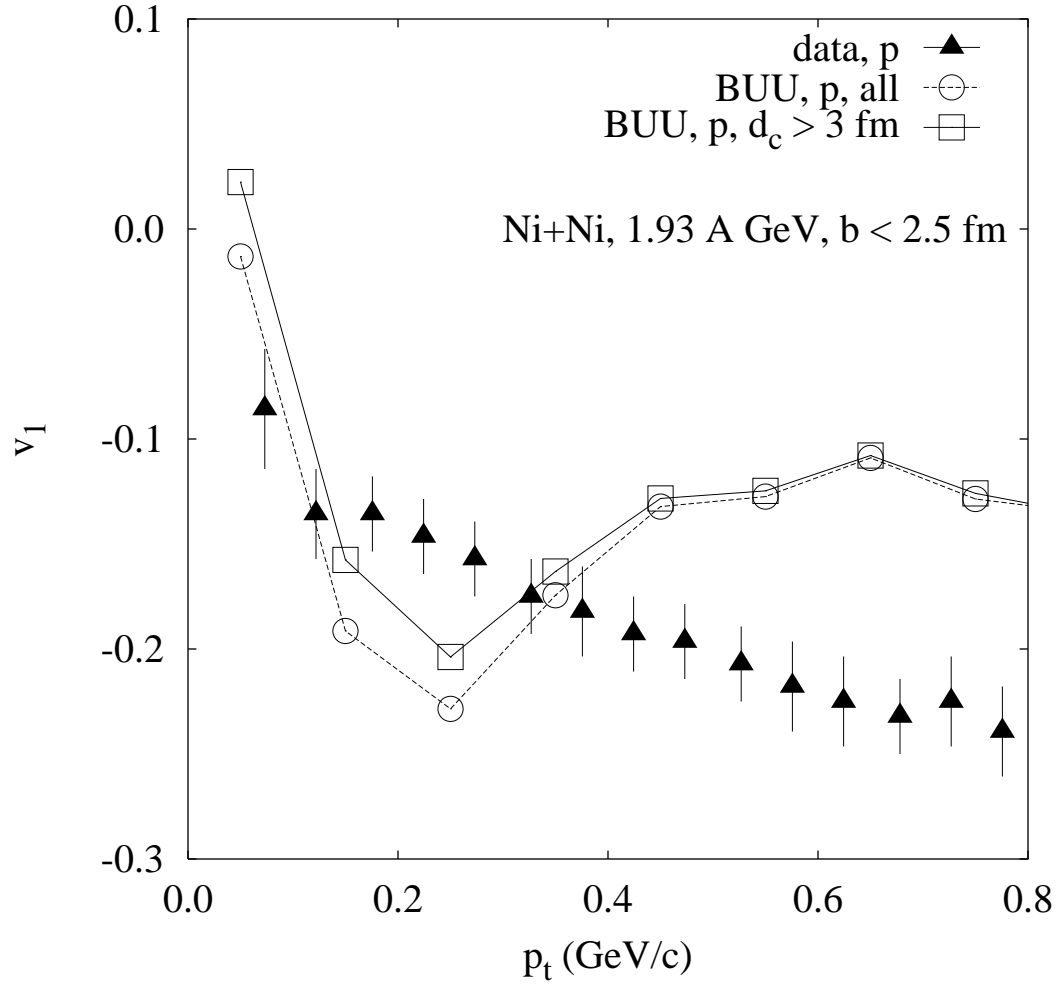


FIG. 12: Proton directed flow vs transverse momentum for collisions Ni+Ni at 1.93 A GeV with $b < 2.5$ fm. Protons are selected in the rapidity range $-1.2 < Y^{(0)} < -0.65$. Data are from Ref. [27].

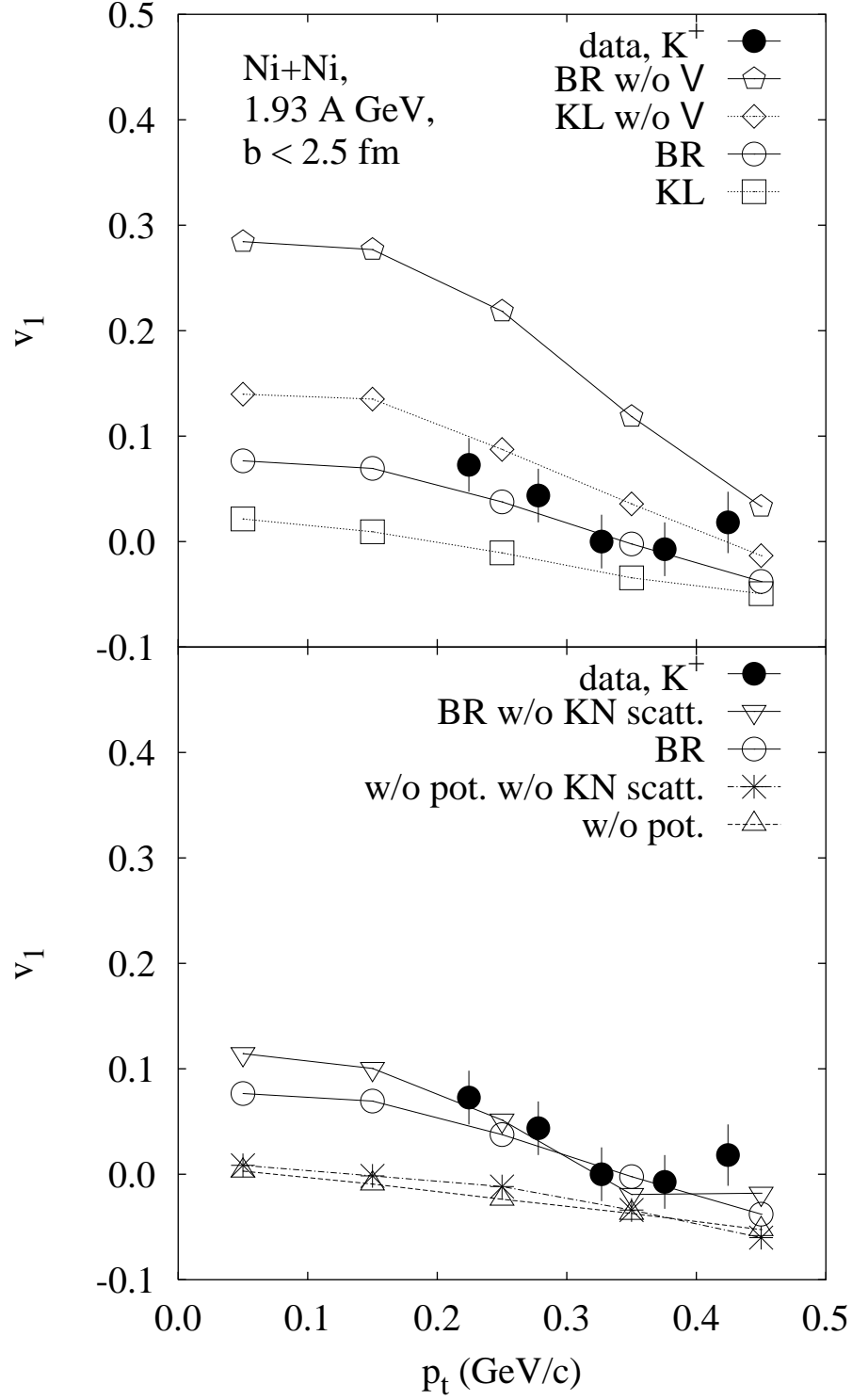


FIG. 13: K^+ directed flow vs transverse momentum for collisions Ni+Ni at 1.93 A GeV with $b < 2.5$ fm. Kaons are selected in the rapidity range $-1.2 < Y^{(0)} < -0.65$. Data are from Ref. [27].

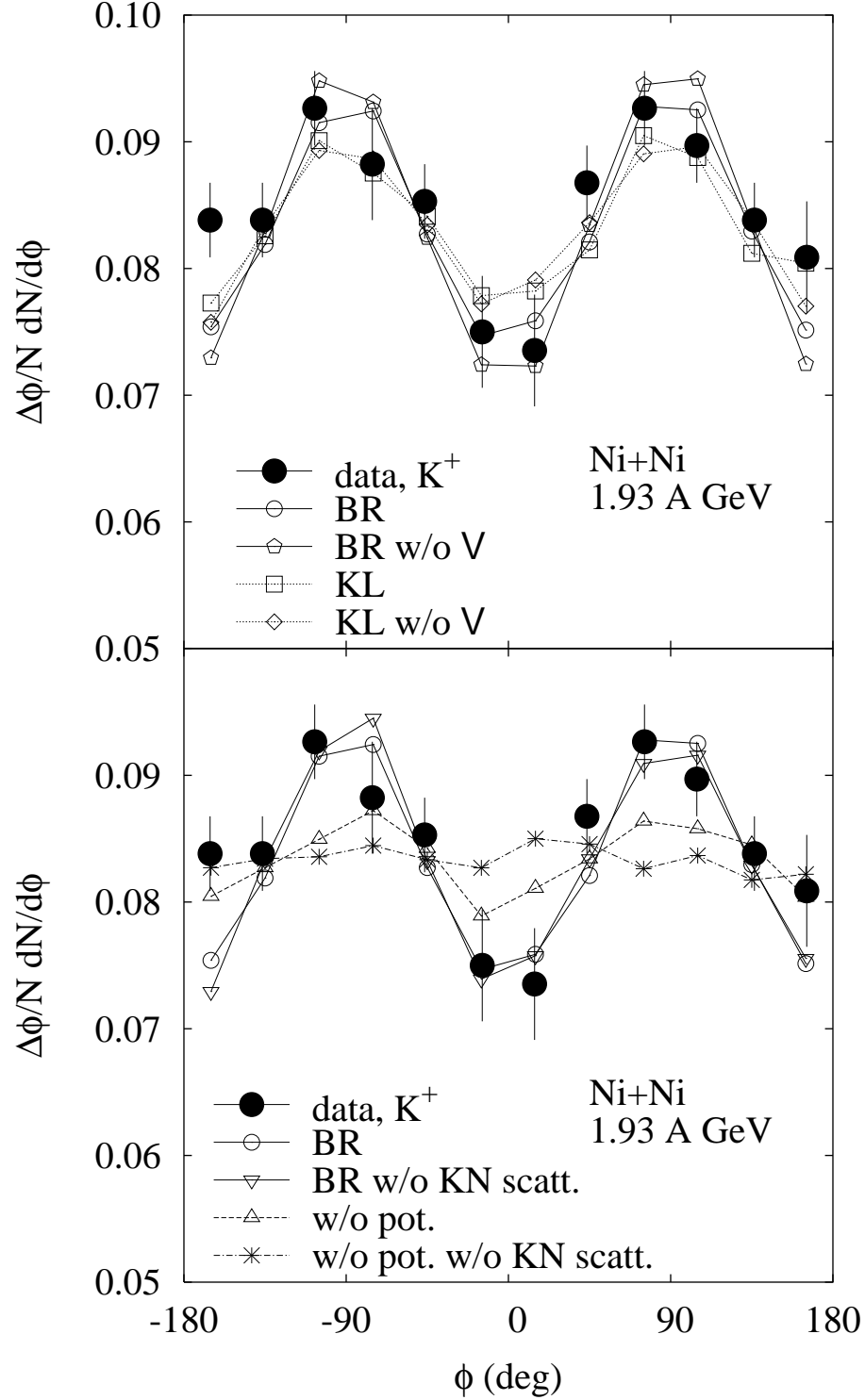


FIG. 14: K^+ azimuthal distributions for semicentral ($b = 4 - 6.5$ fm) Ni+Ni collisions at 1.93 A GeV. Kaons are selected in the rapidity range $|Y^{(0)}| < 0.4$ and in the transverse momentum range $p_t = 0.2 - 0.8$ GeV/c. Different calculations are explained in the text. Data are from Ref. [29].

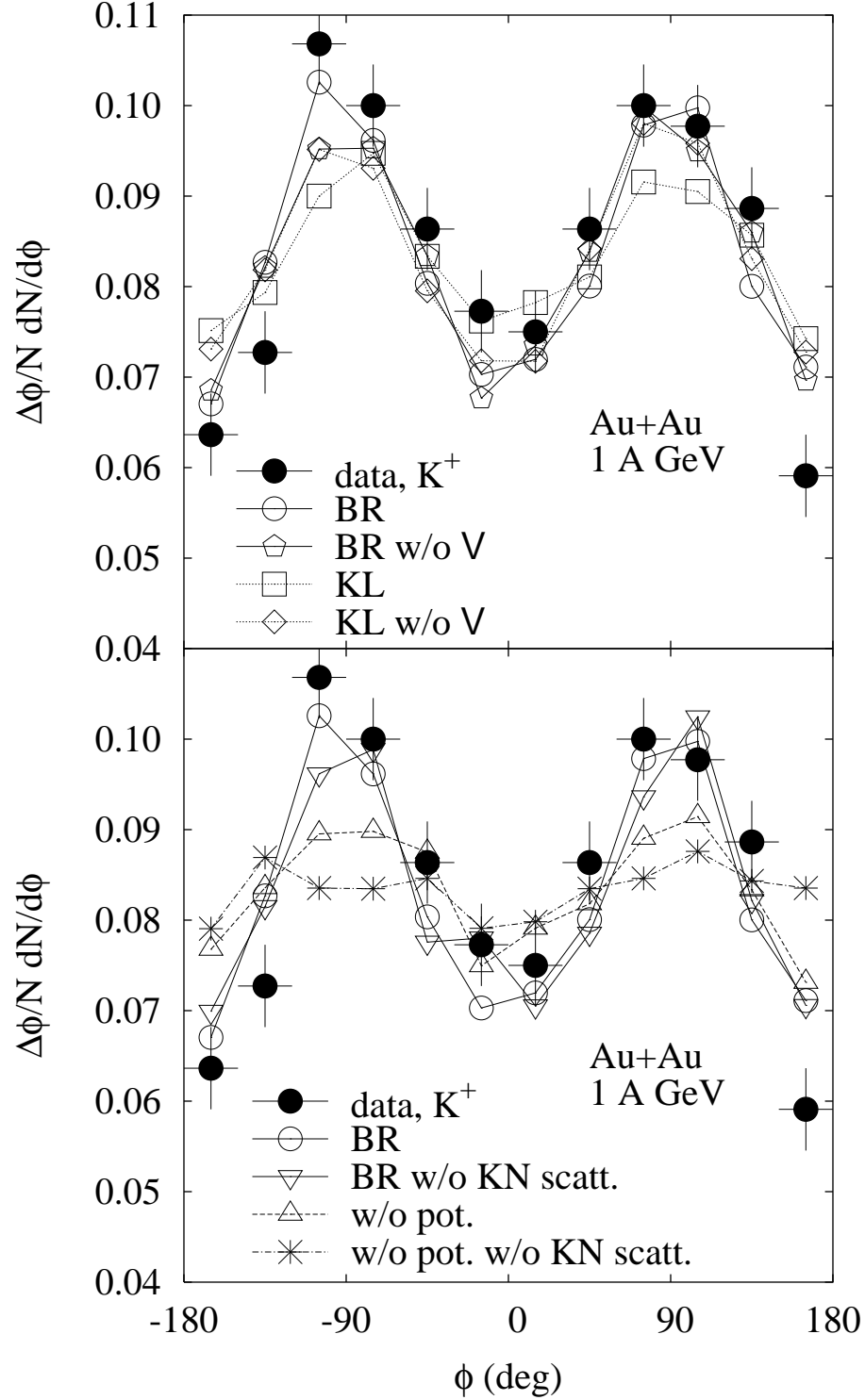


FIG. 15: K^+ azimuthal distributions for semicentral ($b = 5 - 10$ fm) Au+Au collisions at 1 A GeV. Kaons are selected in the rapidity range $|Y^{(0)}| < 0.6$ and in the transverse momentum range $p_t = 0.2 - 0.8$ GeV/c. Different calculations are explained in the text. Data are from Ref. [24].

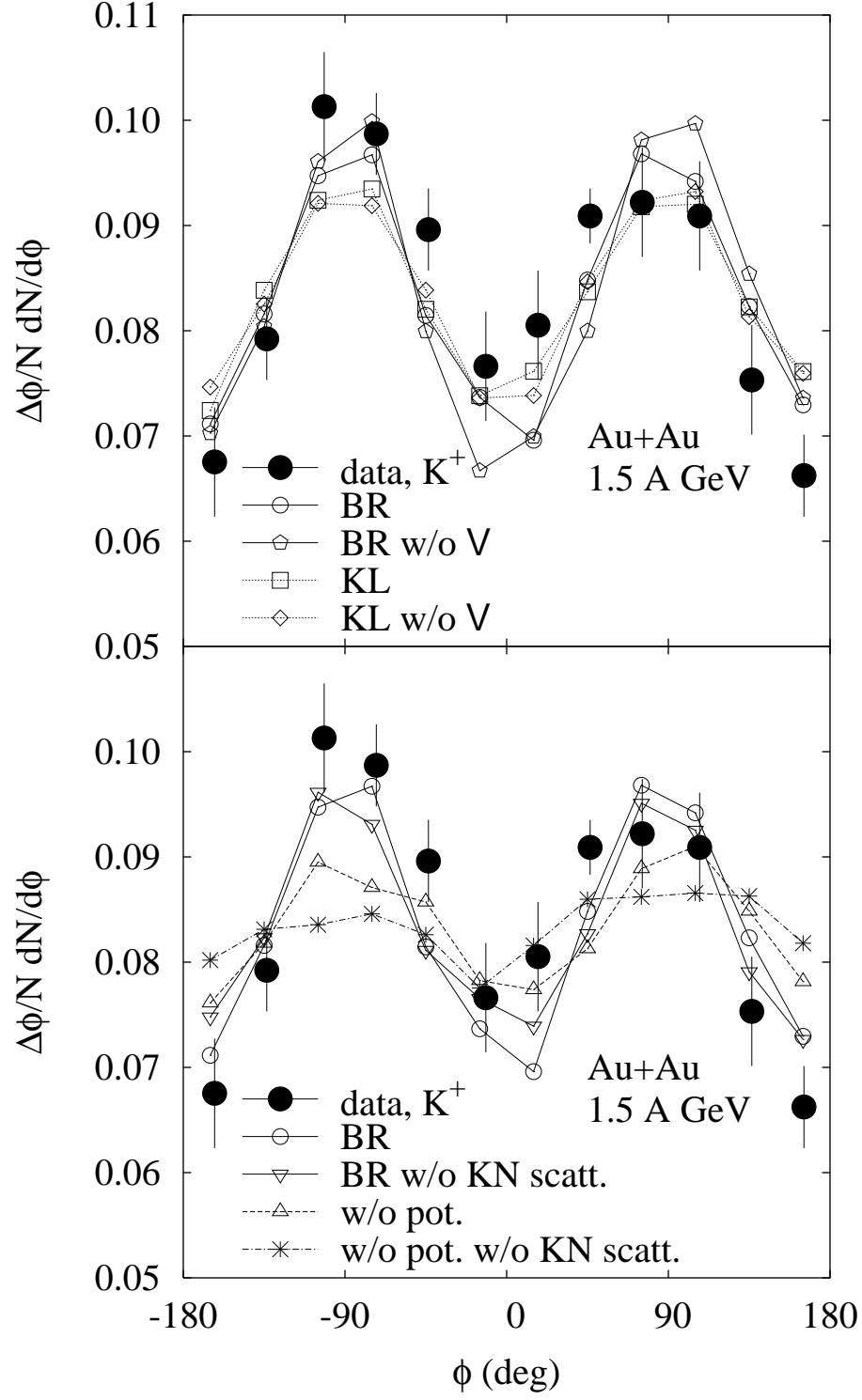


FIG. 16: K^+ azimuthal distributions for semicentral ($b = 6 - 10$ fm) Au+Au collisions at 1.5 A GeV. Kaons are selected in the rapidity range $|Y^{(0)}| < 0.4$ and in the transverse momentum range $p_t = 0.2 - 0.8$ GeV/c. Different calculations are explained in the text. Data are from Ref. [29].

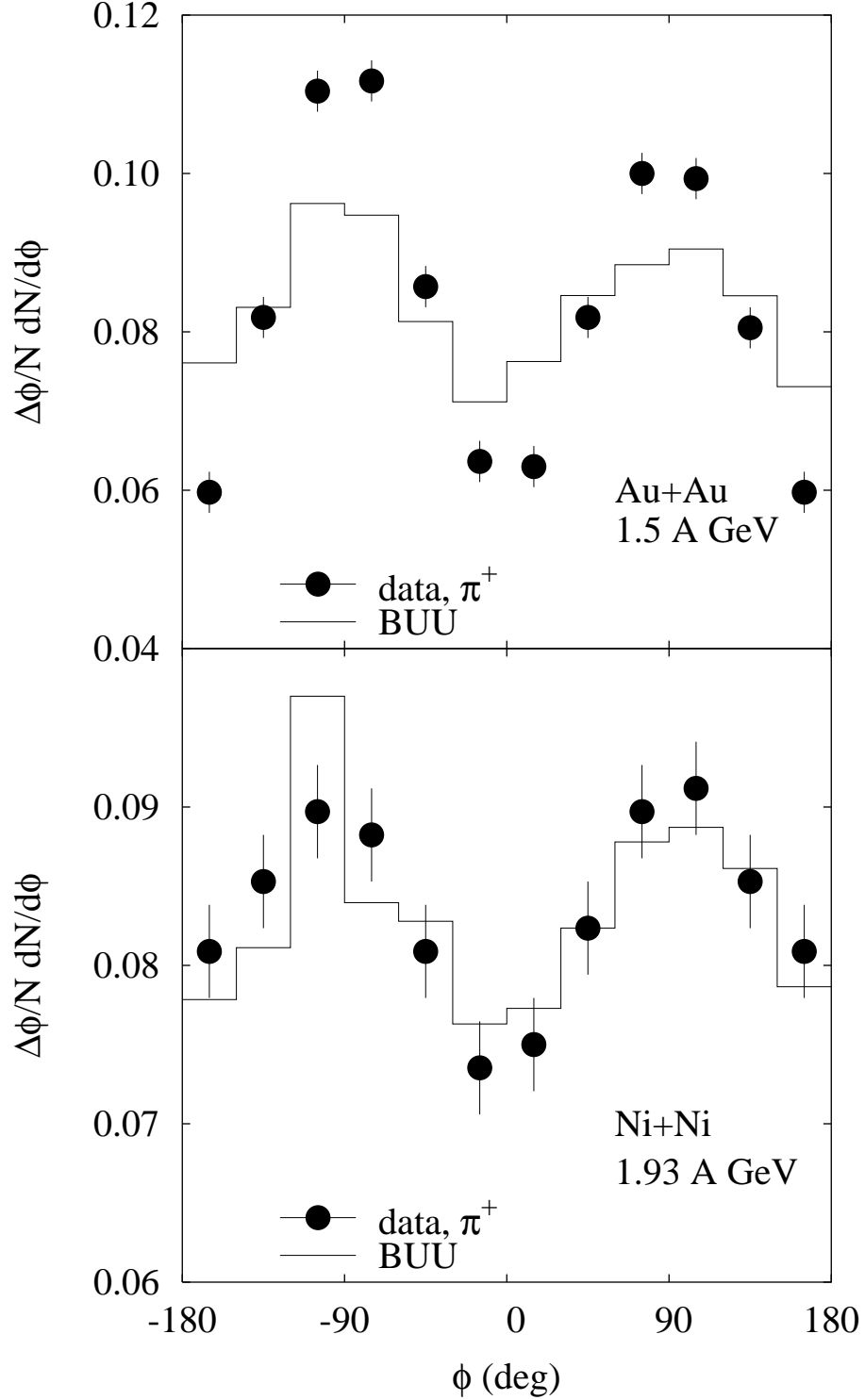


FIG. 17: Azimuthal distributions of π^+ -mesons produced in semicentral ($b = 6 - 10$ fm) Au+Au collisions at 1.5 A GeV (upper panel) and semicentral ($b = 4 - 6.5$ fm) Ni+Ni collisions at 1.93 A GeV (lower panel). Pions are selected in the rapidity range $|Y^{(0)}| < 0.4$ and in the transverse momentum range $p_t = 0.2 - 0.8$ GeV/c. Data are from Ref. [29].